ALTAIR Project for Ultra-Precise Astronomical Photometric Calibration: Design, Production and Testing

by

Diego Gabriel Reyes Olguin
B.Sc., Meritorious Autonomous University of Puebla, 2022

A Thesis Submitted in Partial Fulfillment of the
Requirements for the Degree of

MASTER OF SCIENCE

in the Department of Physics and Astronomy

We acknowledge and respect the Lək̓ʷəŋən (Songhees and Xʷsepsəm/Esquimalt) Peoples on whose territory the university stands, and the Lək̓ʷəŋən and W̱SÁNEĆ Peoples whose historical relationships with the land continue to this day.

ALTAIR Project for Ultra-Precise Astronomical Photometric Calibration: Design, Production and Testing

by

Diego Gabriel Reyes Olguin
B.Sc., Meritorious Autonomous University of Puebla, 2022

Supervisory Committee

Dr. Justin Albert, Supervisor
(Department of Physics and Astronomy)

Dr. Scott Chapman, Departmental Member
(Department of Physics and Astronomy)

Abstract

In quantitative fields, such as astronomy, uncertainties play a huge role. This is particularly true for measurements of dark energy using Type Ia supernovae, where systematics from photometric calibration are the largest source of uncertainty. The ALTAIR (Airborne Laser for Telescopic Atmospheric Interference Reduction) project will tackle this problem using in-situ calibrated light sources at altitudes of ~ 20 km to provide precise and accurate knowledge of optical throughput at a variety of wavelengths, making photometric uncertainty no longer dominant.

This thesis details the design, production, and laboratory testing of ALTAIR payload electronics, with a focus on the custom photodiode readout electronics responsible for monitoring the light source's stability over a wide dynamic range, ranging from picoamperes ($10^{-12}A$) to microamperes ($10^{-6}A$) of photocurrent. The results from linearity testing demonstrate an exceptionally linear response across all operational modes. The transimpedance amplifier shows measured deviations from linearity of less than 0.011% over its operational dynamic range, while the switched-integrator circuits, critical for low-current measurements, exhibit non-linearities of less than 0.0613% of their full-scale range. These results validate a critical subsystem of the ALTAIR payload and confirm that the custom electronics meet the requirements for sub-percent precision photometry.

Table of Contents

List of Tables

List of Figures

Acknowledgements

I would like to thank:

Dr. Justin Albert, For always sharing his vast knowledge with me, and for his endless encouragement and patience as my supervisor.

Nicolas Braam, For his advice and guidance, and for always making time in his schedule to help me with electronics design and testing.

Rachelle, thank you for your love and support, for always listening, and for believing in me.

My friends, Sean, Josh, Bryn, Pranav, Praneet, Daniel, Ruxin, Aviv and Damandeep (not extensive) for being there during both the great moments and the tough ones, and for making me feel welcome from day one.

The mind is its own place and, in itself can make a heaven of hell or a hell of heaven
John Milton

Dedicatoria

Este trabajo está dedicado a mis padres, Javier Reyes y Melissa Olguin por todo su amor, por apoyarme en todas mis decisiones y por ser mi mayor motivación, mis pilares fundamentales.

Chapter 1

Introduction

1.1 Dark Energy

In 1998, observations of distant type Ia supernovae (SNe Ia) revealed that the expansion of the Universe is accelerating, a landmark discovery that reshaped modern physics and cosmology [1, 2]. For this discovery, Saul Perlmutter, Brian P. Schmidt and Adam G. Riess were awarded the Nobel Prize in Physics 2011 [3].

This acceleration implies the existence of a dominant, gravitationally repulsive component of the Universe, termed "dark energy." The primary goal ever since the discovery has been determining the properties of dark energy, and particularly the parameters of the dark energy equation of state as a function of the scale factor of the Universe over cosmic history. If the dark energy equation of state were $p = w\rho$, where p and ρ are respectively the pressure and the density of dark energy in natural units, and the dark energy equation of state parameter w is a constant that is equal to -1 throughout all space and over all cosmic history, then this would be consistent with dark energy being Einstein's cosmological constant. Any observed and confirmed deviations from that picture would suggest new, dynamic physics.

As large scale surveys like the Dark Energy Survey (DES) and the upcoming Vera C. Rubin Observatory's Legacy Survey of Space and Time (LSST) generate vast catalogs of supernovae [4, 5], statistical errors have continued to diminish significantly, making measurements of dark energy further limited by systematic uncertainties (as fractions of total uncertainties) [6, 7, 8]. Progress in understanding dark energy is no longer primarily constrained by the number of supernovae we can find, but by our ability to characterize the calibration effects that are the main source of uncertainty in these new measurements.

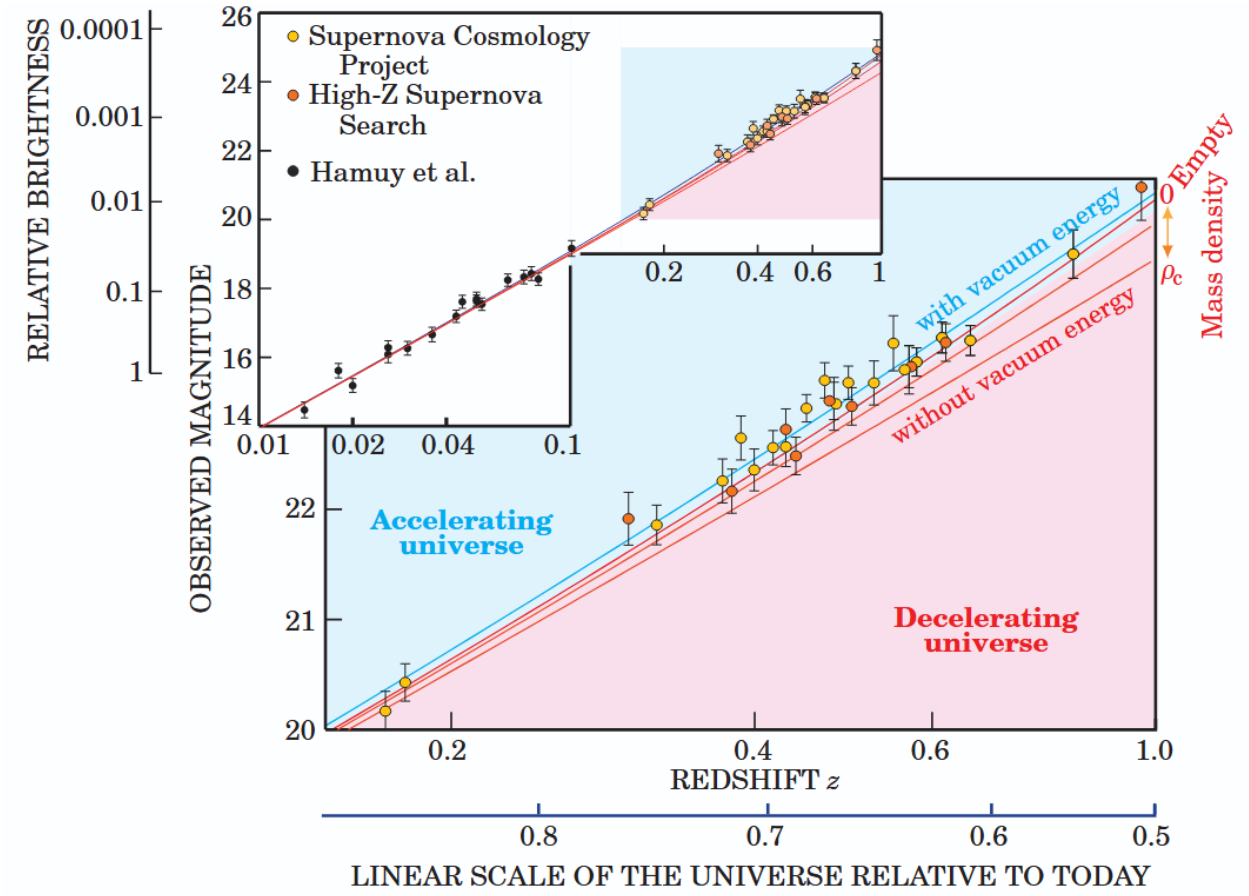

Figure 1.1: Hubble diagram that shows the 1998 results that provided the first evidence for cosmic acceleration. The plot shows the brightness (observed magnitude) of Type Ia supernovae versus their redshift (a measure of distance). The data points from the two teams fall systematically above the line representing a decelerating Universe (red region), indicating they are fainter and thus farther away than expected. The data is best explained by a model that includes an accelerating component, such as vacuum energy (blue region). Figure from Perlmutter (2003) [9].

Although SNe Ia have been the foundational probe for dark energy, they are not the only method for measuring the cosmic expansion history. In particular, Baryon Acoustic Oscillations (BAO) provide an independent cosmological tool: the BAO method uses the residual perturbations in the density of the visible baryonic matter of the Universe, left from adiabatic perturbations in the primordial plasma of the early Universe that oscillated like acoustic waves and attenuated as the Universe expanded [10], as a "standardizable ruler" to map cosmic distances, analogous to the use of SNe Ia as "standardizable candles" in astronomical observations. The key aspect of this technique is that it is a geometric probe that is not limited by the photometric systematics that affect SNe Ia. Recent spectroscopic

surveys, such as the survey performed by the Dark Energy Spectroscopic Instrument (DESI), have utilized this technique to produce the largest three-dimensional maps of the Universe to date [11]. Remarkably, those initial DESI results when combined with other cosmological data show deviation from the cosmological constant model of dark energy depending on the specific SNe Ia dataset used; the preference for a dark energy equation of state that evolves with time can reach a significance of up to $\sim 3.9\sigma$ [12, 13].

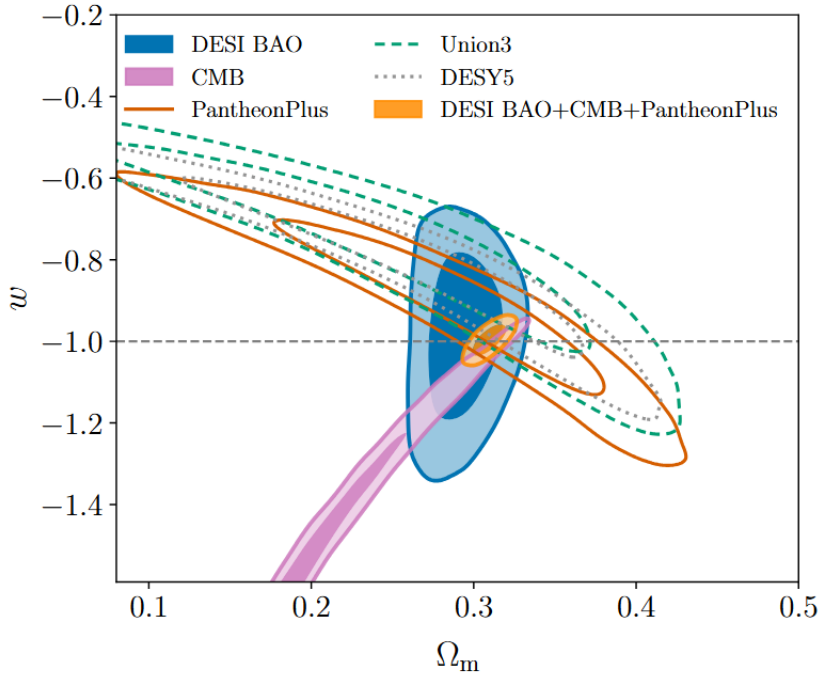

Figure 1.2: Cosmological constraints on the matter density of the Universe (Ω_m) and the dark energy equation of state parameter (w). The plot illustrates the complementarity of different cosmic probes, showing the different constraints from Baryon Acoustic Oscillations (DESI BAO, blue), the Cosmic Microwave Background (CMB, pink), and Type Ia supernovae (Pantheon+, Union3 and DESY5, dark orange, green and grey). The orange contour shows the combined constraint from DESI, CMB and PantheonPlus SNe Ia. All contours show 68% and 95% credible intervals. The value $w = -1$ corresponds to a cosmological constant. Figure from DESI 2024 VI (2025) [12].

Even though the BAO technique is not subject to the photometric calibration systematics of SNe Ia analyses, it has its own set of limitations, primarily systematics from theoretical modeling. The BAO measurements are taken from the spatial distribution of galaxies, which are biased tracers of the underlying matter distribution. This bias evolves over cosmic time and varies across galaxy populations, environments, and halo masses. At late times, the galaxy two-point correlation function becomes increasingly sensitive to the cumulative ef-

fects of galaxy formation physics like stellar feedback, AGN activity, and non-linear structure growth, all of which can distort the measured BAO distance scale [14]. As a result, the observed deviations from $w = -1$ in the DESI analysis may suggest evolving dark energy, but they might also be the effect of poorly constrained theoretical systematics [15]. Since the current amount of tension seen in the DESI data is highly dependent on which SNe Ia compilation is used [13], only entirely separate future SNe Ia measurements of dark energy, with greatly improved calibration resulting in greatly reduced uncertainties from photometry as compared with past SNe Ia dark energy measurements, would and will be able to resolve any fundamental biases due to theoretical systematics in such BAO-based dark energy measurements.

1.2 The Photometric Calibration Barrier

Among the great amount of sources of systematic uncertainty, the largest one that can be improved by more careful measurements is photometric calibration: the precise and accurate determination of uncertainties, and the removal of all known or measured biases, on measurements of the flux, or brightness, of each supernova [16]. The entire method of supernova cosmology relies on comparing the apparent magnitude of a distant supernova to its absolute magnitude to infer its distance. Any error in the flux measurement propagates into an error on the inferred distance and ultimately in the derived cosmological parameters.

Current calibration techniques predominantly rely on observing a network of celestial standard stars. Historically, this has proven difficult to push beyond the so-called "1% precision barrier," which remains a primary obstacle to better constraining the dark energy equation of state [8]. While the atmosphere is a major contributor to this uncertainty, it is not necessarily a fundamental limiting factor for high-precision spectrophotometry. Most atmospheric extinction is dominated by relatively stable components such as Rayleigh scattering, aerosols, and ozone, while more volatile features—such as strong water vapor bands—can be isolated through careful wavelength selection, as demonstrated by Young et al. [17], millimag-level determinations of atmospheric extinction have been achievable through rigorous differential photometry.

Therefore, the shift from celestial standards to SI-traceable measurements is also motivated by the need to bypass the complex metrology chain. Utilizing a well characterized, controlled light source allows for a more direct, fundamental measurement of the combined instrumental and atmospheric throughput.

However, the use of an artificial source introduces its own set of physical constraints, primarily regarding geometric alignment. To accurately characterize the end-to-end throughput

of a telescope, the calibration source must ideally reside in the far field to ensure that incident wavefronts are planar. This is critical because the Point Spread Function (PSF) evolves significantly as a function of distance; to accurately mimic a stellar source, the calibration system must operate at a distance L such that the Fresnel number is less than unity ($F < 1$), defined by the relationship:

$$L > \frac{D^2}{4\lambda} \tag{1.1}$$

where D represents the diameter of the telescope aperture and λ is the operating wavelength. In this regime, the light from the calibration source traverses the telescope optics along the same path as a reference star.

1.3 The ALTAIR Project

This thesis presents a new approach to overcome this fundamental limitation. The ALTAIR (Airborne Laser for Telescopic Atmospheric Interference Reduction) project aims to break the 1% precision barrier by deploying an in-situ calibrated, artificial light source above the bulk of the Earth's atmosphere. By flying a stable, well-characterized light source on a high-altitude balloon platform, ALTAIR will create an "artificial star" of known brightness and color [18, 19].

Observing this source with a ground-based telescope allows for a direct measurement of the combined atmospheric transmission and instrumental throughput at the exact time and location of a science observation. This method decouples the calibration from the inherent uncertainties of celestial standards, allowing a reduction of photometric uncertainties by an order of magnitude to the 0.1% level [19]. This approach builds on previous work that demonstrated the viability of using satellite-mounted lasers, such as the one aboard the CALIPSO satellite, to precisely measure atmospheric extinction [18].

1.4 Thesis Outline

This thesis documents my contribution to the ALTAIR project, focusing on the design, assembly, and validation of eletronics of the balloon-borne payload.

- **Chapter 2** Describes in detail the open problem, it reviews the use of Type Ia supernovae as standardizable candles with a specific focus on the dominant role of photometric calibration uncertainty as quantified by recent cosmological surveys.

- **Chapter 3** Presents the new solution developed in this work: the ALTAIR project's

high-precision photodiode readout board. This chapter details the design process of electronics and justifies the selection of critical components, such as the switched-integrator ICs and low-thermal-EMF relays, and explains the implementation of low-noise PCB layout techniques like guard rings.

- **Chapter 4** Describes the experiments performed to validate the hardware and presents the key results. This chapter details the methodology for the laboratory characterization of the readout electronics.

- **Chapter 5** Contains a restatement of the claims and results of the thesis, summarizing the demonstrated performance of the custom electronics. It also enumerates avenues of future work for further development of the concept and its applications.

Chapter 2

The Problem to be Solved

2.1 The Accelerating Universe and Type Ia Supernovae

The modern cosmological paradigm is built upon the discovery that the expansion of the Universe is accelerating [1, 2]. This conclusion was first drawn from observations of high-z type Ia supernovae (SNe Ia), a class of stellar explosions that are physically distinct from the core collapse supernovae of massive stars. SNe Ia are understood to be the result of a thermonuclear explosion of a compact, carbon-oxygen white dwarf star in a close binary system [6]. In the prevailing model, the white dwarf accretes mass from its companion, causing it to approach the Chandrasekhar mass limit of $\sim$1.4 solar masses, which is the maximum mass (for a non-rotating compact star) that can be supported by electron degeneracy pressure. As it nears this critical threshold, the temperatures and densities in the core become sufficient to trigger runaway carbon burning, which causes the star to very rapidly collapse implosionally and then fully disrupt in a matter of seconds. The visible light from the resulting explosion is not from the initial shockwave, but is powered by the radioactive decay chain:^{56}Ni $\rightarrow$ ^{56}Co $\rightarrow$ ^{56}Fe. While the exact progenitor systems and explosion mechanisms are still an area of active research, this model allows Type Ia supernovae to be excellent standardizable candle candidates. [6].

2.1.1 The Friedmann-Lemaître-Robertson-Walker Metric

The mathematical description of an expanding Universe is grounded in Einstein's theory of General Relativity. By assuming that on large scales, the Universe is both homogeneous and isotropic, one can derive a metric that describes the geometry of spacetime [20]. This solution is known as the Friedmann-Lemaître-Robertson-Walker (FLRW) metric:

$$ds^2 = -c^2dt^2 + a^2(t)\left[\frac{dr^2}{1-kr^2} + r^2(d\theta^2 + \sin^2\theta d\phi^2)\right]. \tag{2.1}$$

The term ds^2 is the squared differential spacetime interval, where ds represents the four-dimensional "distance" between two infinitesimally close events. The term c is the constant speed of light, and dt is the differential interval of cosmic time, which is the time measured by an observer at rest with the cosmic expansion. The crucial term is $a(t)$, the dimensionless scale factor, which is a function of time, that describes the relative expansion of the Universe. The parameter k is the dimensionless curvature constant which specifies the overall geometry of space: $k = +1$ corresponds to a closed, spherical geometry; $k = 0$ to a flat, Euclidean geometry; and $k = -1$ to an open, hyperbolic geometry [20].

The evolution of the scale factor is governed by the Friedmann equations, which are derived by applying Einstein's field equations to the FLRW metric. The first Friedmann equation relates the expansion rate of the Universe to its energy content:

$$\left(\frac{\dot{a}}{a}\right)^2 = \frac{8\pi G}{3c^2}\epsilon - \frac{kc^2}{a^2}, \tag{2.2}$$

where $\dot{a}$ is the time derivative of the scale factor, $H \equiv \dot{a}/a$ is the Hubble parameter, ϵ is the total energy density of the Universe (including matter, radiation, and dark energy), and G is the gravitational constant [20].

The Friedmann acceleration equation describes how the expansion rate changes over time:

$$\frac{\ddot{a}}{a} = -\frac{4\pi G}{3c^2}\left(\epsilon + 3P\right). \tag{2.3}$$

Here, $\ddot{a}$ is the second time derivative of the scale factor and P is the pressure of the cosmic fluid. This equation shows that for normal matter and radiation (where $\epsilon > 0$ and $P \geq 0$), gravity is attractive and causes the expansion to decelerate ($\ddot{a} < 0$). The discovery of cosmic acceleration ($\ddot{a} > 0$) implies the existence of a component with sufficiently negative pressure (dark energy) to overcome gravity and drive the expansion [20].

The geometry of the Universe is directly linked to its total energy density. For a given expansion rate H, there is a critical density, ϵ_c, required for the spatial geometry to be flat ($k = 0$):

$$\epsilon_c(t) = \frac{3c^2 H(t)^2}{8\pi G}. \tag{2.4}$$

The ratio of the actual density to the critical density defines the density parameter, $\Omega(t) = \epsilon(t)/\epsilon_c(t)$. An $\Omega > 1$ corresponds to a closed Universe, while $\Omega < 1$ corresponds to an open one. Measuring the history of $a(t)$ by observing distant objects allows determination of these parameters.

2.2 Standardizable Candles

To measure the expansion history of the Universe, $a(t)$, one must be able to determine the distances to objects at various redshifts. This is accomplished using the cosmic distance ladder, a succession of methods where each "rung" is used to calibrate the next, more distant one. The foundational principle for measuring great astronomical distances is the concept of a "standard candle."

A standard candle is an astronomical object with a known, or predictable, intrinsic luminosity (L). By measuring the object's apparent brightness, or flux (f), as seen from Earth, its luminosity distance (d_L) can be calculated using the inverse-square law for light [20]:

$$f = \frac{L}{4\pi d_L^2}. \tag{2.5}$$

In astronomy, brightness is measured on a logarithmic magnitude scale. The relationship between apparent magnitude (m) and absolute magnitude (M) is given by the distance modulus equation. The absolute magnitude M is formally defined as the apparent magnitude an object would have if it were observed from a standard distance of exactly 10 parsecs. This definition leads to the distance modulus equation [20]:

$$m - M = 5 \log_{10} \left(\frac{d_L}{10 \text{ pc}} \right). \tag{2.6}$$

The challenge lies in identifying classes of objects that are truly standard and in accurately calibrating their absolute magnitudes.

The first rungs of the distance ladder are built within our local cosmic neighborhood. Distances to the nearest stars can be measured directly using trigonometric parallax. These parallax measurements are then used to calibrate the luminosity of the first set of standard candles, most notably Cepheid variable stars. Discovered by Henrietta Swan Leavitt, Cepheids are pulsating stars whose period of variability is directly related to their intrinsic luminosity [21]. By measuring the pulsation period of a distant Cepheid, its absolute magnitude can be determined, and thus its distance can be calculated. It was through the use of Cepheids that Edwin Hubble first established that other galaxies existed far beyond our own Milky Way [22].

However, to probe the Universe on cosmological scales and measure the effects of dark energy, brighter standard candles are required. For this reason, astronomers turned to Type Ia supernovae.

2.3 Type Ia Supernovae as Standardizable Candles

The utility of SNe Ia as cosmological probes stems from their nature as "standardizable candles." While not all SNe Ia have the exact same intrinsic peak luminosity, their brightness is strongly correlated with observable properties of their brightness over time. Correcting for these variations can standardize the intrinsic luminosities of SNe Ia to a precision of approximately $0.12 - 0.16$ mag, which corresponds to a distance measurement precision of $\sim 4\%$ [23, 24].

Figure 2.1: A before and during comparison of the Pinwheel Galaxy (M101), showing the appearance of the bright type Ia supernova SN 2011fe. During their peak brightness, supernova can sometimes even outshine their host galaxy (although this is clearly not the case here: M101 is a particularly large, bright host). Image credit: B. J. Fulton (LCOGT)/PTF/STScI, as presented in Cowen (2011) [25].

This process of standardization relies on two empirical correlations. The first is the Phillips relation, which demonstrates that intrinsically brighter SNe Ia have broader light curves, fading more slowly after reaching their peak brightness than their dimmer counterparts [26]. The second is the Tripp relation, which shows that SNe Ia that appear redder at peak brightness are intrinsically fainter than those that are bluer [27].

These empirical laws are implemented through sophisticated light-curve fitting models, such as SALT2, MLCS2k2, or SNooPy, which are trained on large, high-quality datasets of

nearby supernovae [28, 29, 30]. For a distant supernova, a fitter takes the observed multi-band photometric data points and determines the apparent peak magnitude, a light-curve shape (or "stretch") parameter, and a color parameter. Applying corrections based on the shape and color parameters yields a standardized magnitude with an associated uncertainty, which is then used to calculate the luminosity distance and place the supernova on a Hubble diagram.

2.4 The Leading Uncertainties

Dedicated surveys since the turn of the millennium have increased the sample of SNe Ia from a few dozen to thousands [24], a sample size that has been further expanded by the Dark Energy Survey (DES) 5-year results [31] and the Union3 compilation [32]. This has dramatically reduced the statistical uncertainties on cosmological parameters. However, this progress is changing the science from being statistics limited to systematics limited [8]. The dominant source of error in measuring the properties of dark energy is no longer the size of the supernova sample, but systematic effects of instrumental artifacts and atmospheric transmission.

Photometric calibration is the process of converting instrumental measurements into physical flux units on a standardized system. It is consistently the largest non-astrophysical source of systematic uncertainty in modern analyses [16, 8]. Achieving the sub-percent precision required for next-generation surveys demands a deep understanding of every component in the observational chain.

The total systematic error budget in a modern supernova cosmology analysis is a complex mix of individual uncertainties, summarized in Table 2.1. The Joint Light-curve Analysis (JLA) [33], a major compilation of SDSS-II and SNLS supernovae, provides a quantitative breakdown of these components. The table details the contribution of various error sources to the uncertainty in the matter density parameter, Ω_m. This detailed accounting allows for a direct comparison of the relative impact of systematic effects versus statistical limitations.

An analysis of this error budget reveals the dominant role of calibration. By examining the individual contributions to the uncertainty budget, we can assess the total impact of each category. Calibration is by far the largest systematic source, contributing an uncertainty of $\sigma_x(\Omega_m) = 0.0203$. This single factor accounts for approximately 36.7% of the total variance ($\sigma^2(\Omega_m)$), which is significantly larger than the next leading systematic contributors: Milky Way extinction and Light-curve modeling. Notably, the calibration uncertainty is comparable in magnitude to the total statistical uncertainty ($\sigma_{stat} = 0.0241$, accounting for 51.6% of the variance). This quantitative breakdown demonstrates that photometric calibration

is the leading source of systematic uncertainty in this analysis. It is precisely this type of challenge that provides the direct motivation for the ALTAIR project, as the development of its hardware and software is targeted at mitigating these dominant calibration uncertainties.

Table 2.1: Contribution of various sources of measurement uncertainties to the uncertainty in Ω_m. The table lists the uncertainty contribution $\sigma_x(\Omega_m)$ and the percentage contribution to the total variance $\sigma^2(\Omega_m)$. Adapted from Betoule et al. (2014) [33].

Uncertainty sources	$\sigma_x(\Omega_m)$	**% of** $\sigma^2(\Omega_m)$
Calibration	0.0203	36.7
Milky Way extinction	0.0072	4.6
Light-curve model	0.0069	4.3
Bias corrections	0.0040	1.4
Host relation[a]	0.0038	1.3
Contamination	0.0008	0.1
Peculiar velocity	0.0007	0.0
Stat	0.0241	51.6

[a]Includes evolution of the β and color correction parameters.

2.4.1 Uncertainties on Optical Throughput: Atmospheric and Instrumentational

For any ground-based observatory the Earth's atmosphere is the first optical interface; the atmosphere absorbs and scatters light in a wavelength dependent manner, a process known as atmospheric extinction. This transmission function varies with time and direction on the sky due to changes in airmass, aerosols, water vapor, and ozone content, due to this complexity, fully characterizing this atmospheric transmission along the telescope's line of sight is one of the primary challenges to achieving sub-percent photometry [8]. Atmosphere transmission variability is certainly a very important effect for photometric calibration to incorporate; importantly, however, the variability in total optical throughput (and the resulting uncertainties and biases on the calculated throughput) tend in fact to be dominated by instrumental and detector effects, rather than by atmospheric variability.

After passing through the atmosphere, light is collected by a telescope and recorded by a camera, the precise transmission of the telescope optics and the quantum efficiency of the detector are also complex functions of wavelength and temperature that result in a combined instrument response function that must be known precisely to accurately convert detected photo-electrons into an incident flux [8]. Furthermore, because cosmological analyses must combine supernovae from different surveys to span a wide redshift range, data from mul-

tiple telescopes with unique instrumental signatures must be placed on a single, consistent photometric system. Efforts like the "Supercal" analysis can have systematic discrepancies between the zeropoints of 1%–2%, which propagate to up to 5% systematic errors in SN distance. This systematic error in distance can then result in an average offset of 2%–3% in w.[34]

2.4.2 The Fundamental Limit of Celestial Standards

The traditional method for anchoring a photometric system is to observe a set of standard stars whose brightness has been previously measured. However, this technique faces a fundamental precision limit of approximately 1% [18]. This limit arises from multiple factors: stars themselves can be intrinsically variable; the network of primary standards is sparse and often much brighter than the distant supernovae being studied, introducing non-linearity uncertainty and the process of transferring the calibration from a primary standard to secondary standards across the sky introduces cumulative errors [8]. Critically, the flux distributions of the best stellar standards are not based on direct laboratory measurements but on calculated model atmospheres [16]. This entire metrology chain is susceptible to systematic errors that are difficult to quantify at the sub-percent level [8]. Man-made light sources, in contrast, can be measured in a laboratory to a precision up to 100 times better than standard stellar sources [18]. To make further progress, a new approach is required that can go over the inherent limitations of stellar calibrators and deliver laboratory-grade precision[8].

Chapter 3

New Approaches and Solutions

The fundamental limitation of celestial standard stars, as detailed in Chapter 2, necessitates an improvement in photometric calibration. To break the 1% precision barrier, a new approach must be developed that decouples the calibration process from the inherent uncertainties of astrophysical sources. The ALTAIR project offers a solution by introducing a recoverable, "artificial star". This chapter details the ALTAIR concept, from its foundational principles to the elements of the system designed and tested in this work. It describes what is fundamentally new in this approach, what is built upon previous research, and how the system operates in practice to achieve its goal of sub-percent photometric precision.

Instead of relying on the inferred flux of a distant star, ALTAIR creates a calibration source whose properties are measured in-situ. This is achieved by deploying a lightweight, self-contained, and stable light source on a high-altitude balloon platform, positioning it above the majority of the atmosphere allowing to characterize the atmospheric extinction, and due to the nature of the platform, it can be easily transported and launched when and were needed to provide the calibration source at the exact time of capturing an exposure with a ground telescope.

3.0.1 ALTAIR within Past and Future Calibration Efforts

The idea of using artificial sources for calibration is not entirely new. Stubbs & Tonry (2006) proposed using in-situ tunable lasers and calibrated photodiodes to map the throughput of a telescope system on the ground, a technique that addresses instrumental response but not atmospheric transmission [8]. Building on this, the viability of using an airborne source to characterize the atmosphere was demonstrated through a campaign of observations of the $532nm$ pulsed laser aboard the CALIPSO satellite. These observations proved that a light source above Earth's atmosphere with known output could be used to directly measure atmospheric extinction [18]. CALIPSO helped demonstrating the principle but it was an ex-

periment of opportunity using a satellite with a different primary mission. ALTAIR is part of a new generation of projects aimed at providing artificial calibration sources above the atmosphere. A significant complementary effort is the upcoming NASA Pioneers Landolt mission. Landolt is a 12U small satellite that will orbit at approximately 35,786 kilometers to shine a set of NIST-traceable, flux-calibrated lasers at ground observatories, with a primary goal of achieving 0.5% absolute flux calibration at a few discrete wavelengths chosen to overlap with the Rubin and Roman observatories [35]. The satellite platform of Landolt presents a different set of strengths and limitations when compared to ALTAIR's balloon platform. Landolt will be positioned much higher above Earth's atmosphere, allowing it to provide calibration that accounts for the full atmospheric column. However, the Landolt mission is not expected to be available until 2030, is significantly more costly, and its geostationary orbit restricts its accessibility to a fixed region of the sky, mainly providing persistent coverage for specific telescopes in the Americas. Critically, its calibration is fixed at launch and cannot be returned to Earth for re-verification. In contrast, ALTAIR offers a cheaper, more flexible system that can provide calibration for a variety of wavelengths for a wider range of observatories worldwide, and its recoverability allows for crucial re-validation of the calibration after recovery.

The ALTAIR project, together with projects like Landolt, synergizes and represents a critical step forward by developing dedicated platforms specifically designed for photometric calibration that will include a multi-wavelength source, continuous real time monitoring, the capability of maintaining itself above a region of Earth for extended periods of time and recoverability in the case of ALTAIR, and the capacity to account for absorption from molecules in the upper atmospheric layers in the case of Landolt.

3.0.2 What is Totally New

The truly novel contribution of the ALTAIR project is the use of a low-cost, steerable, and recoverable high-altitude balloon platform. This approach is very different from the extremely expensive and more permanent satellite missions and offers several advantages. One of the most significant ones is the ability to recover the payload after a flight. Unlike a satellite, the ALTAIR payload is designed to be recovered after each flight (Figure 3.1). This allows for post-flight laboratory analysis, enabling direct measurement of any degradation or changes in the instrumentation. This ability to compare pre- and post-flight laboratory calibrations is a unique feature that eliminates possible long-term drift uncertainties, to protect the instrumentation, a parachute is used to slow the descent and reduce landing speed. And an onboard propulsion system will help maneuvering and stabilizing the payload

during descent, lowering the risk of damaging landings.

Furthermore, this platform provides high cost-effectiveness and operational flexibility. The use of high-altitude balloons and largely commercial-off-the-shelf components makes the system orders of magnitude cheaper than a dedicated satellite mission, making it highly accessible and allows for rapid development cycles and frequent flight opportunities. The balloon platform can be launched on demand and, using its onboard propulsion, can be maneuvered to remain persistently over a specific observatory, providing crucial calibration data precisely when and where it is needed for a given scientific observation.

3.1 System Architecture and Operation

The ALTAIR system is a complete, end to end solution consisting of the airborne scientific payload, a ground control station, and operational software that integrates them. This section describes the components and functionality of the system, using the prototype developed in this thesis as a working example.

3.1.1 The Airborne Payload

The ALTAIR payload is a lightweight integrated system designed to operate in the environment of the stratosphere at altitudes of $\sim$ 20km. It consists of three primary subsystems: the light source, the power system, and the control and monitoring electronics.

The Light Source

The core of the scientific payload is the artificial star itself. It consists of modular system with four thermoelectrically cooled laser diodes at discrete wavelengths (440, 532, 635, and 690 nm) that are fed into an integrating sphere. This produces a spatially uniform, Lambertian light source. The output of this sphere is continuously monitored in-flight by a SI-traceable calibrated photodiode, providing a real-time measurement of the source's brightness.

The Power System

The payload is designed for long-duration flights and is powered by a system of lightweight, flexible solar panels and a rechargeable Li-Po battery. The power system was tested extensively both in the laboratory under simulated solar conditions (Figure 3.3) and outdoors (Figure 3.4). A custom-designed solar battery charger board (Figure 3.2) was designed to allow charging throughout a flight via the 3 P3-30W solar panels mounted on top of the ballon.

Figure 3.1: The ALTAIR high-altitude balloon being inflated during preparations for the September 11, 2025 test flight by the team at McGill University.

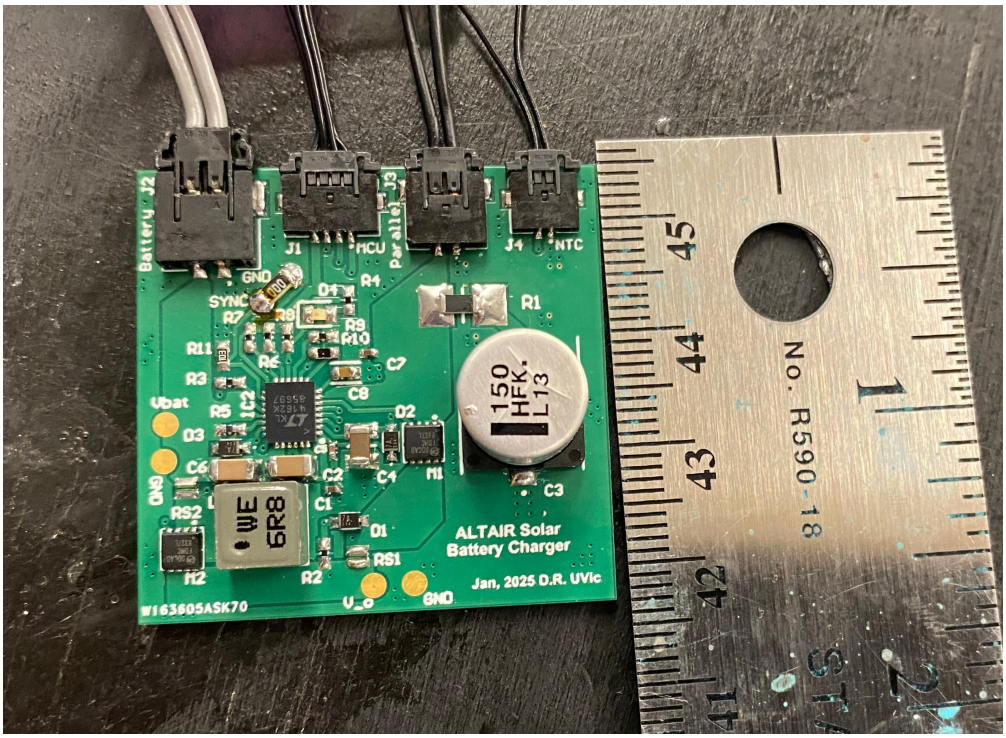

Figure 3.2: The custom-designed ALTAIR Solar Battery Charger circuit board, responsible for managing power from the solar panels to the onboard battery.

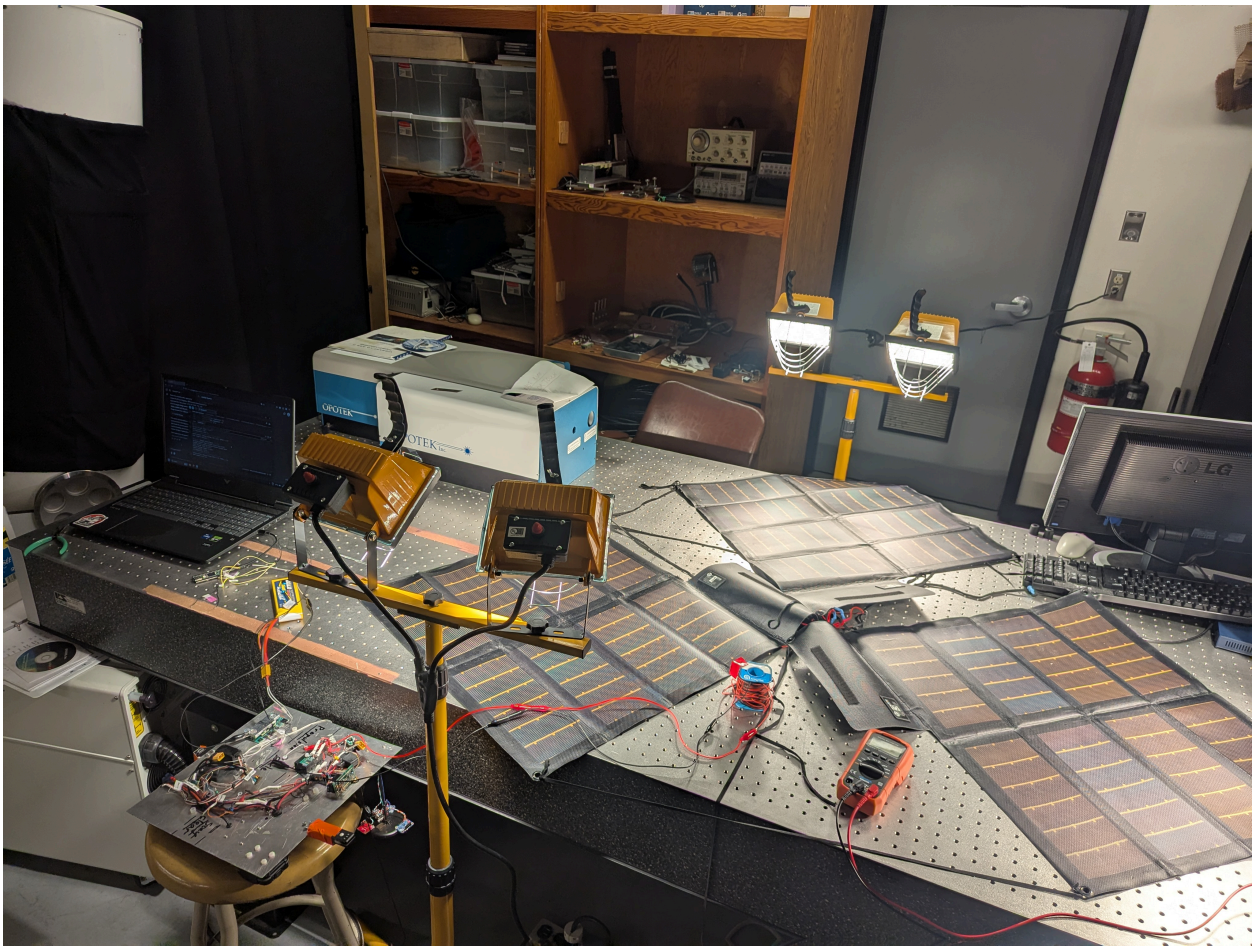

Figure 3.3: Laboratory setup for testing the ALTAIR solar power system. Multiple solar panels are illuminated by halogen lamps to simulate solar insolation and test the performance of the charging electronics.

Figure 3.4: Outdoor testing of the custom battery charging circuit with the flexible solar panels that will be used on ALTAIR.

Photodiode Readout Electronics

This subsection will focus on the photodiode readout electronics that I have designed (in addition to my design of the solar power battery charging electronics mentioned previously). Please note that a comprehensive summary of all ALTAIR onboard electronics will be provided in a later publication. The precision sensory electronic readout within the payload is contained on a set of custom-designed printed circuit boards (PCBs) that read out the photocurrent measurements from the onboard precision monitoring photodiodes. The photodiodes are, in turn, mounted on the onboard integrating sphere. The development of these boards involved an iterative design process. An early prototype of the readout board (Figure 3.5, purple board) was found to be inadequate as it lacked the necessary integrator options for low-light measurements and was physically too large for the compact payload design. This led to a complete redesign, resulting in the current set of PD Readout boards. This new system is a modular, stackable set of three distinct but similar boards, designated Sergeant, Soldier, and Specialist.

The Sergeant board is the primary data acquisition and control unit. It is responsible for amplifying or integrating, and digitizing the signal from the monitoring photodiode. The Soldier (Figure 3.6) and Specialist (Figure 3.7) boards are secondary boards that can be stacked on top of the Sergeant or each other in any combination, but they also amplify or integrate, and digitize the signal from their respective photodiodes. The stacking allows for the control of two boards over a single bus connection from the main payload computer to the Sergeant board.

A key feature of this stackable design is the ability to perform simultaneous measurements of two diffferent photodiodes within the same IC. The Sergeant board is populated with a dual-channel ACF2101 integrator, which utilizes highly matched internal capacitors. This allows for the simultaneous integration and reading of signals from two different photodiodes, nominally, one connected to the Sergeant board and one connected to the stacked Soldier board. To transfer the sensitive, low-level photodiode signal from the secondary board to the Sergeant board without introducing noise, the chosen connection method was spring-loaded pogo pins, used to carry both the high-impedance signal trace and its corresponding guard trace between the boards. This ensures that the guard ring's protection is maintained across the physical gap between the PCBs.

Design and Component Selection for the PD Readout Board

The primary function of the PD Readout board is to accurately measure the photocurrent from the onboard monitoring photodiode over a wide dynamic range, ranging from picoam-

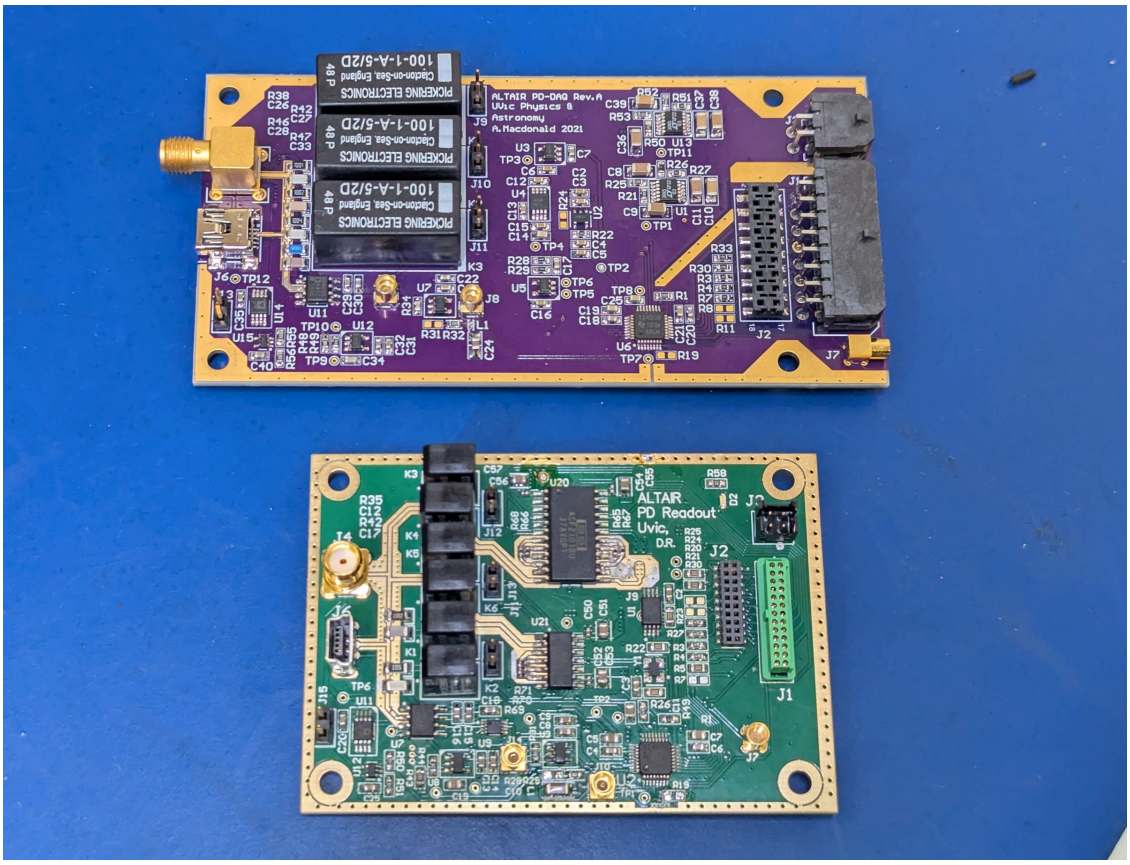

Figure 3.5: The evolution of the ALTAIR readout electronics. The purple board (top) is the initial prototype, which was replaced by the smaller, more capable green PD Readout board (bottom, of Sergeant type, please see text) designed as part of this work.

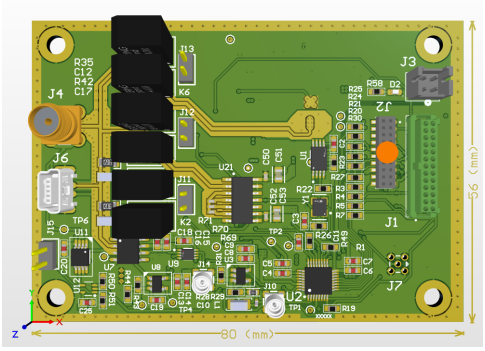

Figure 3.6: A 3D rendering of the Soldier board, one of the modular components of the PD Readout system, designed to stack with the Sergeant board.

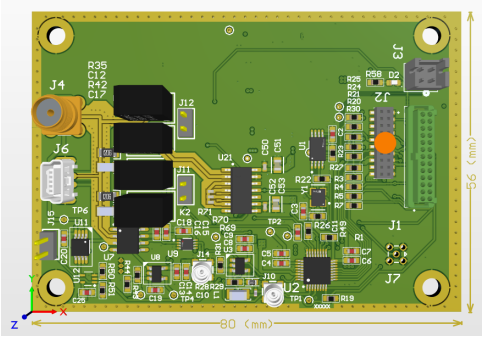

Figure 3.7: A 3D rendering of the Specialist board, a variant of the PD Readout, allowing for remote sensor configurations.

peres ($10^{-12}A$) to microamperes ($10^{-6}A$) of photocurrent.

For continuous wave operation of the laser modules, yielding photocurrents in the range

of hundreds of nanoamps to hundreds of microamps a transimpedance amplifier (TIA) is sufficient. However, for the extremely low photocurrents expected in the integrators operational modes, a simple TIA would require impractically large feedback resistors, which can be susceptible to noise and thermal drift and the instantaneous nature of TIA circuits could lead to variations if used along PWM (pulse width modulation), as discrete sampling may capture the signal during an 'off' state. To address this, the new board design incorporates switched integrator circuits, which measure charge accumulated over a set period rather than an instantaneous current measurement. This also allows for operation of the laser diodes with PWM to simulate fainter astronomical targets.

Two candidate integrator ICs were identified for this purpose: the single-channel IVC102 and the dual-channel ACF2101. The ACF2101 presented a significant advantage due to its two channels and internally matched integration capacitors, making it ideal for applications requiring simultaneous readout of two different photodiodes. To validate their performance and integration requirements before committing them to the final complex PCB layout, simple, dedicated test boards were designed and produced for both the IVC102 (Figure 3.8) and the ACF2101 (Figure 3.9).

Figure 3.8: The dedicated test board designed to characterize the performance of the single-channel IVC102 switched integrator.

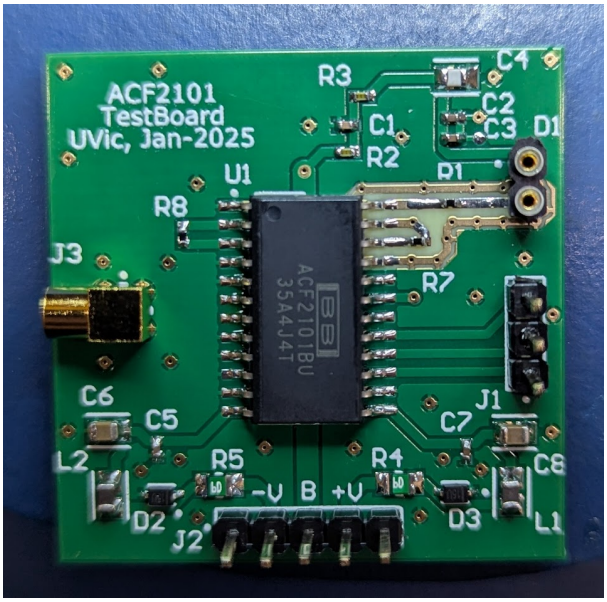

Figure 3.9: The dedicated test board for the dual-channel ACF2101 switched integrator, which features two input channels.

Achieving precision at very low current levels (picoamperes or less) requires meticulous attention to PCB layout to mitigate sources of error. One of the significant error sources

is surface leakage current, where stray currents can travel across the PCB substrate and contaminate the high-impedance input of the amplifier. To prevent this, a guard ring was implemented in the design. As seen on the test boards (Figures 3.8, 3.9) and the final design (Figure 3.10), the guard is a conductive trace that completely encircles the sensitive input trace but is not electrically connected to it. This guard trace is actively driven to the same potential as the input trace making it so there is no potential difference between the input trace and the guard, this prohibits PCB parasitic and environmental factors from contributing non-negligible leakages that can affect measurements in a sensitive circuit [36].

Another critical source of error in low-level DC measurements is thermal electromotive force (EMF), an unwanted voltage generated at the junction of dissimilar metals due to temperature gradients. In this system, channel switching requires relays; however, thermal dissipation from the energized coil creates a temperature differential across the internal junctions of the reed switch (iron-nickel alloy), generating an offset voltage on the order of microvolts. While small, this EMF is a significant error source when measuring signals that can be themselves in or close to the microvolt range. To mitigate this, a test was performed to select the optimal relay configuration with the lowest thermal EMF, using specialized low EMF reed relays and following the methodology described by Pickering Electronics [37]. Several configurations were tested, including a single Pickering 100-1-A-5/2D relay (Figure A.1), a single 118-1-A-5/2D relay, and two 118-1-A-5/2D relays in both parallel and series configurations (Figure A.2).

The results of these tests, shown in Figure A.3, demonstrate that across a range of coil voltages, the configuration of two 118-1-A-5/2D relays consistently produced the lowest thermal EMF, measuring as low as 0.3 μV. This represents an order of magnitude improvement over the single relay options, which generated EMFs as high as 9.4 μV, and implementing two 118-1-A-5/2D relays in series per channel takes less PCB space than a single 100-1-A-5/2D relay per channel. Based on this, the series relay configuration was selected for the final PD Readout board design. These careful component selections and low-noise design considerations were incorporated into the redesigned PD Readout board.

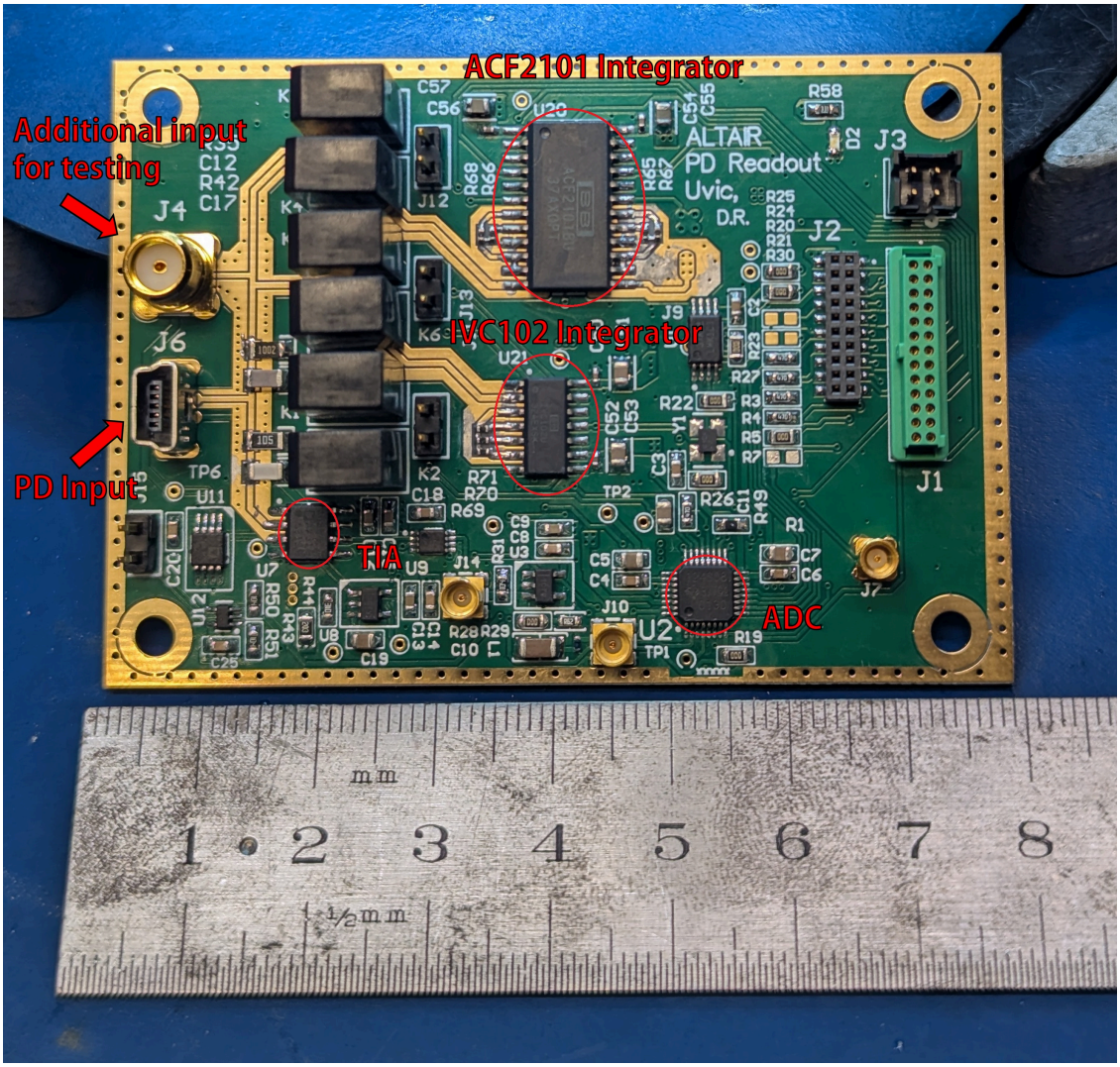

Figure 3.10: A detailed view of the ALTAIR Photodiode (PD) Readout board. This board processes the signal from the SI-traceable calibrated photodiode that monitors the light source output, providing the crucial in-flight flux measurement.

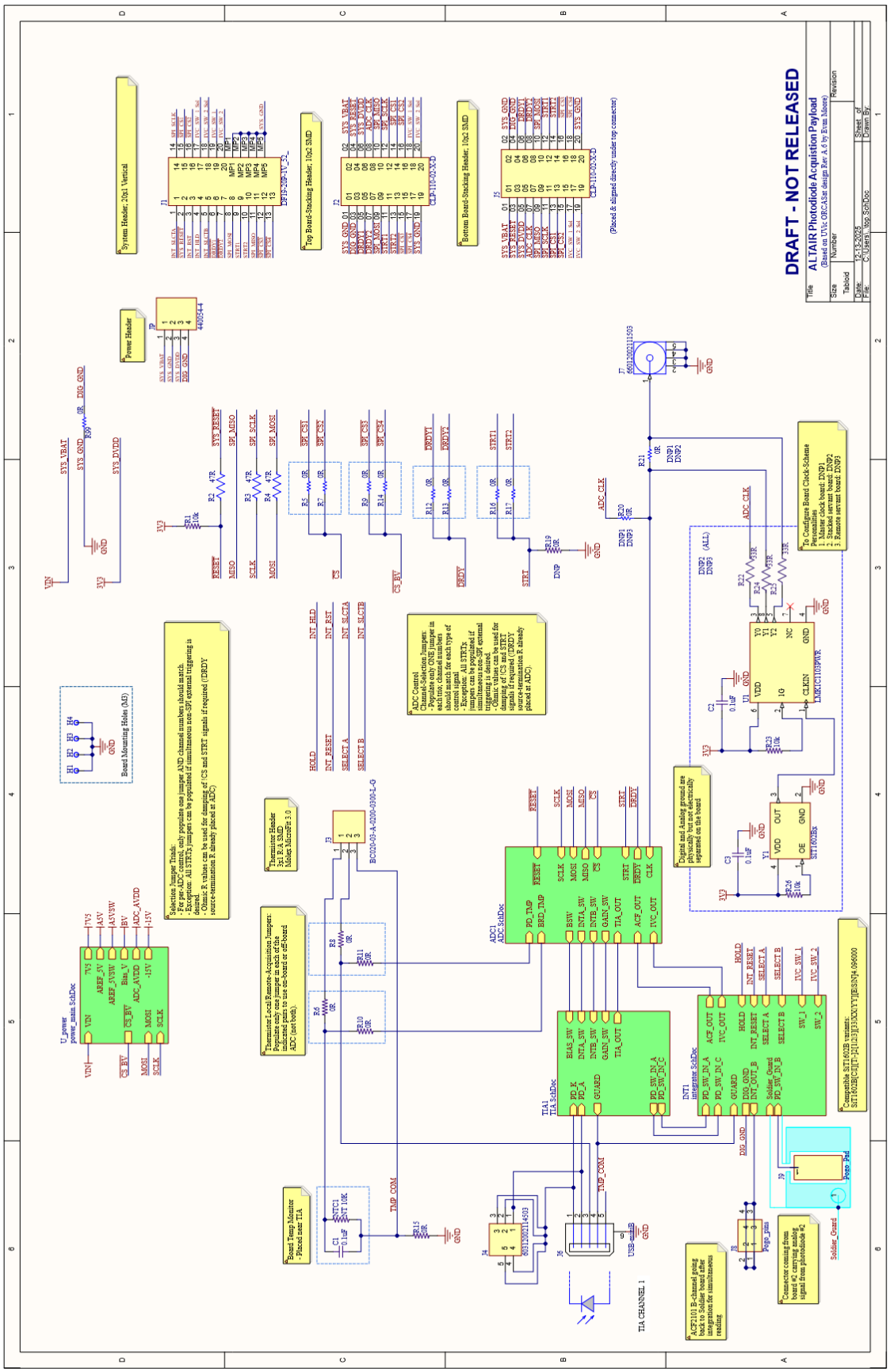

Figure 3.11: Schematic Overview showing interconnections between the photodiode readout sub-circuits.

3.1.2 Ground Operations and Control Software

All aspects of an ALTAIR flight are managed from a portable ground station running a custom-built software suite that is constantly being updated and mantained. The ALTAIR Integrated Flight Control, Operation, Monitoring, and Simulation System (AIFCOMSS) (Figure 3.12).

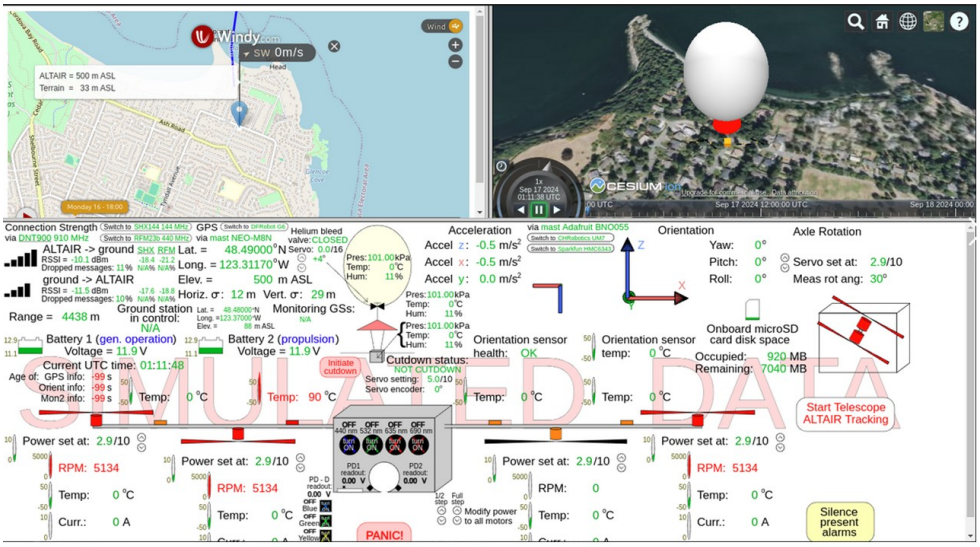

Figure 3.12: A screenshot of the AIFCOMSS software interface. This graphical user interface continues to evolve; it provides real-time telemetry, payload control, and navigational data, integrating all aspects of mission operations.

AIFCOMSS is responsible for:

- **Command and Control:** Operators can remotely turn the science lasers on and off, adjust their power levels, and control other payload functions.
- **Vehicle Health and Monitoring:** The software provides a real-time display of telemetry from the payload, including GPS location, altitude, battery voltage, component temperatures, and sensor readings.
- **Navigation and Prediction:** AIFCOMSS is integrated with the CUSF balloon flight prediction code, utilizing NOAA wind prediction data that allows for real-time flight path visualization and prediction to aid in station-keeping and recovery operations.
- **Safety:** Critical functions such as the flight termination (cutdown) mechanism.

Figure 3.13: The portable ALTAIR ground station during a field test conducted by the McGill engineering team. The system will allow for complete monitoring and control of the airborne payload.

3.1.3 The Calibration Procedure

The ALTAIR system provides a direct, end-to-end calibration of the entire observational system (atmosphere and telescope). A typical calibration sequence proceeds as follows:

1. The payload undergoes pre-flight calibration in the laboratory, where its light output is measured against a SI-traceable standard.

2. The balloon is launched and ascends to its operational altitude of ∼20km.

3. Using AIFCOMSS, the operator sets the balloon to a position within the field of view of the ground-based telescope to be calibrated.

4. The science lasers are activated. The ground telescope then observes the payload, which appears as a point-like artificial star of known, stable, and actively monitored brightness.

5. The telescope measures the apparent magnitude of the ALTAIR source. By comparing the flux received at the telescope's detector to the known flux being emitted by the payload (as reported by the onboard photodiode readout), a direct measurement of the total system throughput, including atmospheric extinction, is obtained for each of the laser wavelengths.

6. Following the observation, the payload is commanded to descend and is recovered and then returned to the laboratory for postflight re-validation, where its calibration and the performance of its components are re-measured to account for any potential changes or degradation.

This procedure has been successfully demonstrated in prototype form. Figure 3.15 shows an image of an ALTAIR prototype payload captured by a collaborating team at McGill University, confirming the viability of observing the airborne source with astronomical instrumentation. Note that the motion of the ALTAIR payload during the exposure results in the light source appearing as a streak, as seen in Figure 3.15. To address the specific challenges of analyzing these non-point sources, ALTAIR collaborator Joshua Goodeve developed a dedicated software package called `StreakTools`[38]. This code is capable of performing accurate photometry on light streaks and also provides the functionality to inject simulated streaks into astronomical exposures.

Figure 3.14 shows telemetry data from the September 11 flight by the McGill University team, drawing the complete flight path from launch near Montreal, ascent to apogee where the balloon bursts, and descent. Marking a successful operational control and tracking of

the payload throughout a launch and provides crucial position and orientation data of the payload at the time of taking the scientific exposure.

The validation of the payload's electronic subsystems, which is critical to ensuring the precision of the onboard flux monitoring, is detailed in Chapter 4.

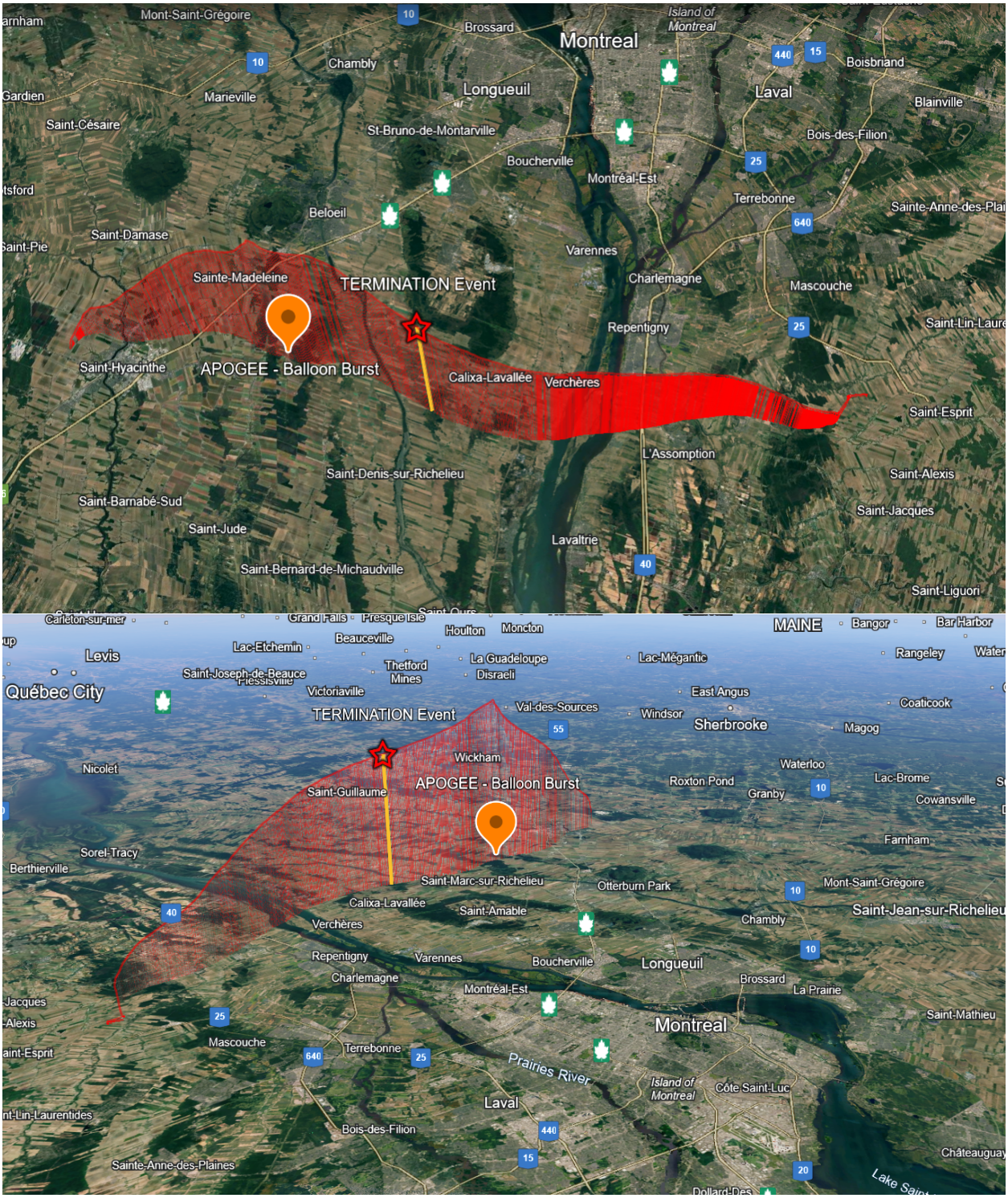

Figure 3.14: Telemetry data from a successful engineering flight conducted with the McGill University team. The top and bottom panels show the overall flight trajectory, including the balloon burst event when the balloon reaches its maximum altitude and bursts and the termination event, which is a command sent from the ground station to mechanically detach the payload from the balloon, initiating its descent.

Figure 3.15: A 5-second exposure of an ALTAIR prototype payload in flight, captured by the team at McGill University on September 11, 2025. The image was taken with a ZWO ASI585MC Pro camera and a Sigma 17-50mm lens (at 17mm, f/2.8). The streak is the airborne light source.

Chapter 4

Experiments and Evaluation

A successful implementation of the ALTAIR concept depends on the performance of its components. To achieve the goal of 0.1% photometric precision, every element in the measurement chain must be understood and characterized to a high level of precision. This chapter details the experiments performed to validate the custom electronics designed for this thesis, focusing on the PD Readout board. It describes the experimental methodology, presents a thorough analysis of the measurement uncertainties, and evaluates the results to demonstrate that the hardware meets the requirements for precision cosmology.

4.1 Component Validation: PD Readout Board TIA Linearity

A critical component of the ALTAIR payload is the PD Readout board, which must accurately convert the tiny photocurrent from the in-flight monitoring PD into a digital value. A key requirement for this conversion is that the amplification electronics exhibit high linearity. Non-linearity in the electronics would directly translate into a systematic error in the measured brightness of the light source, propagating to the resulting w. This section details the testing of the transimpedance amplifier (TIA) channels of the PD Readout board.

4.1.1 Experimental Methodology

To precisely measure the linearity of the TIA circuit, a stable and accurately known input current source is required. A PDVS 2 Mini v1.6 precision voltage source was used to apply a known voltage across a Caddock 1776-C6815 Decade Resistor. This setup, by Ohm's law ($I = V/R$), produces a stable and precisely known input current, which is then fed into the input of the TIA circuit on the PD Readout board.

The test was conducted by systematically sweeping the voltage from the source, generating a range of input currents spanning the operational dynamic range of the TIA. At each

step, the output voltage from the TIA was measured using a Keithley DMM6500 precision digital multimeter. The experiment was performed for the two TIA gain settings, 1 MΩ and 10 kΩ, to validate performance across different operational modes. The 1 MΩ setting ensures high gain for low-magnitude photocurrents, while the 10 kΩ setting provides a lower gain path to prevent saturation for currents up to hundreds of microamperes.

4.1.2 Uncertainty Analysis

Evaluation of the TIA linearity requires distinguishing between random noise sources, which drive point-to-point scatter, and correlated systematic errors, which act as a fixed bias across the measurement set.

Input Current Uncertainty

The input current $I_{in} = V_{src}/R_{nom}$ carries uncertainties from the voltage source and the resistor. We categorize these as:

- **Random ($\sigma_{I,rand}$):** Dominated by the PDVS voltage noise floor and resolution ($\delta_{pdvs} \approx 50\,\mu$V). This term contributes to the observed scatter.
- **Systematic ($\sigma_{I,sys}$):** Dominated by the resistor tolerance δ_{tol} (0.1% for 1 MΩ and 0.01% for 10 kΩ). This error is correlated; while the exact mean value is unknown within the tolerance band, it remains fixed for all points in a single sweep.

Output Voltage Uncertainty

Similarly, the uncertainty in the measured output voltage σ_V is partitioned:

- **Random ($\sigma_{V,rand}$):** Includes the TIA Johnson noise ($V_{n,rms}$), transient thermal EMFs (V_{emf}), and DMM resolution. These fluctuate between individual readings.
- **Systematic ($\sigma_{V,sys}$):** Includes the TIA input offset voltage (V_{os}), input bias current (I_B), and the DMM's calibration accuracy. These terms contribute a constant offset or scaling bias to every data point.

4.1.3 Results and Evaluation

The data were analyzed using Orthogonal Distance Regression (ODR) to account for uncertainties in both input current and output voltage. The linear model used is $V_{out} =$

$m \cdot I_{in} + b$. For simplicity in the regression weighting, the random and systematic components described in Section 4.1.2 were combined in quadrature to define the total uncertainty ($\sigma_{total} = \sqrt{\sigma_{rand}^2 + \sigma_{sys}^2}$).

Figure 4.1 and Figure 4.2 present the results for the 1 MΩ and 10 kΩ gain stages. The residuals demonstrate excellent linearity across the dynamic range. These results provide strong empirical validation that the PD Readout board is capable of measuring photocurrents with the high degree of linearity required.

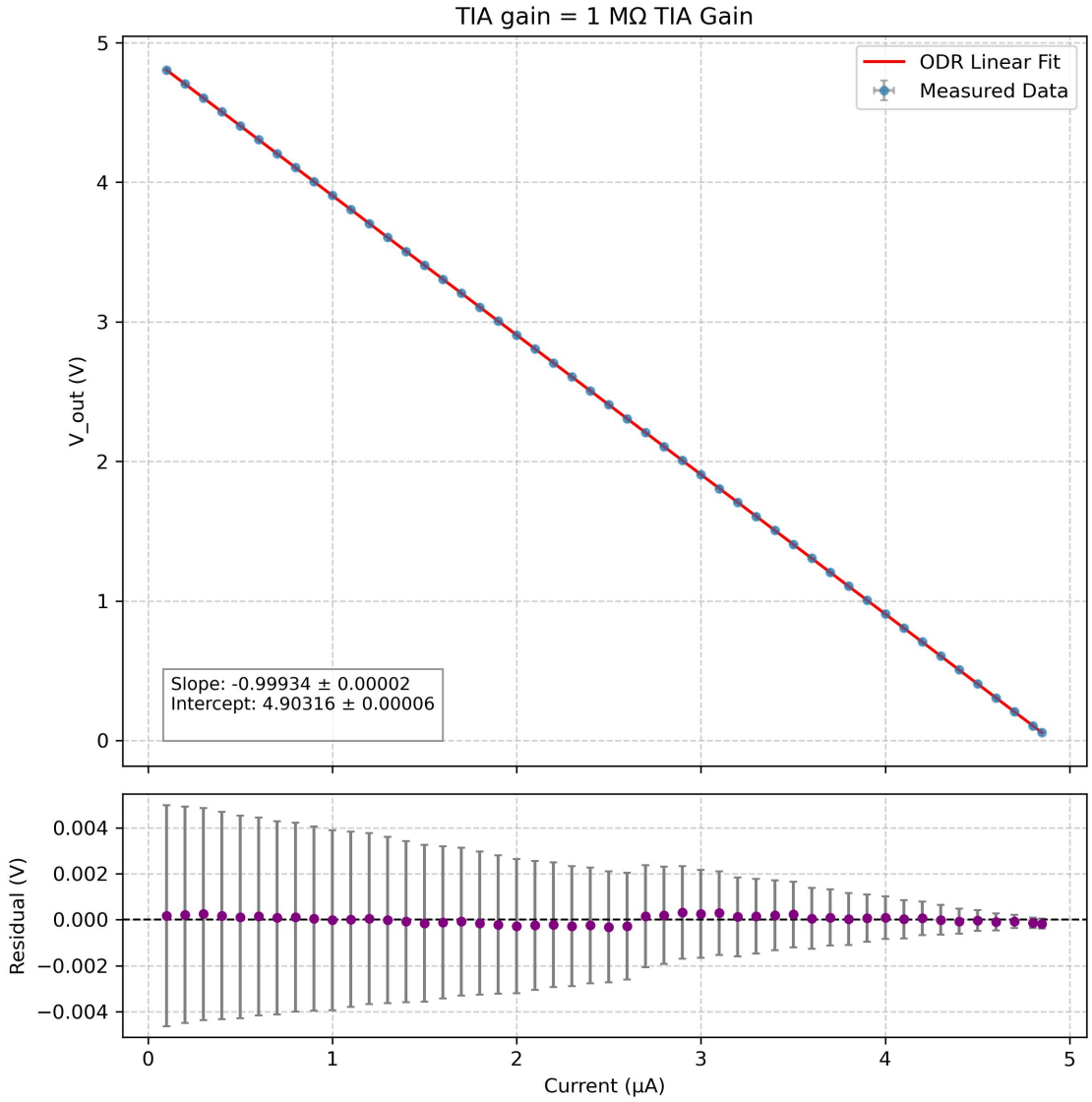

Figure 4.1: Linearity test results for the TIA circuit configured for a gain of 1 MΩ. The top panel shows the measured output voltage versus input current with the ODR linear fit. The bottom panel shows the residuals. Note that error bars reflect the total uncertainty budget including correlated systematic terms.

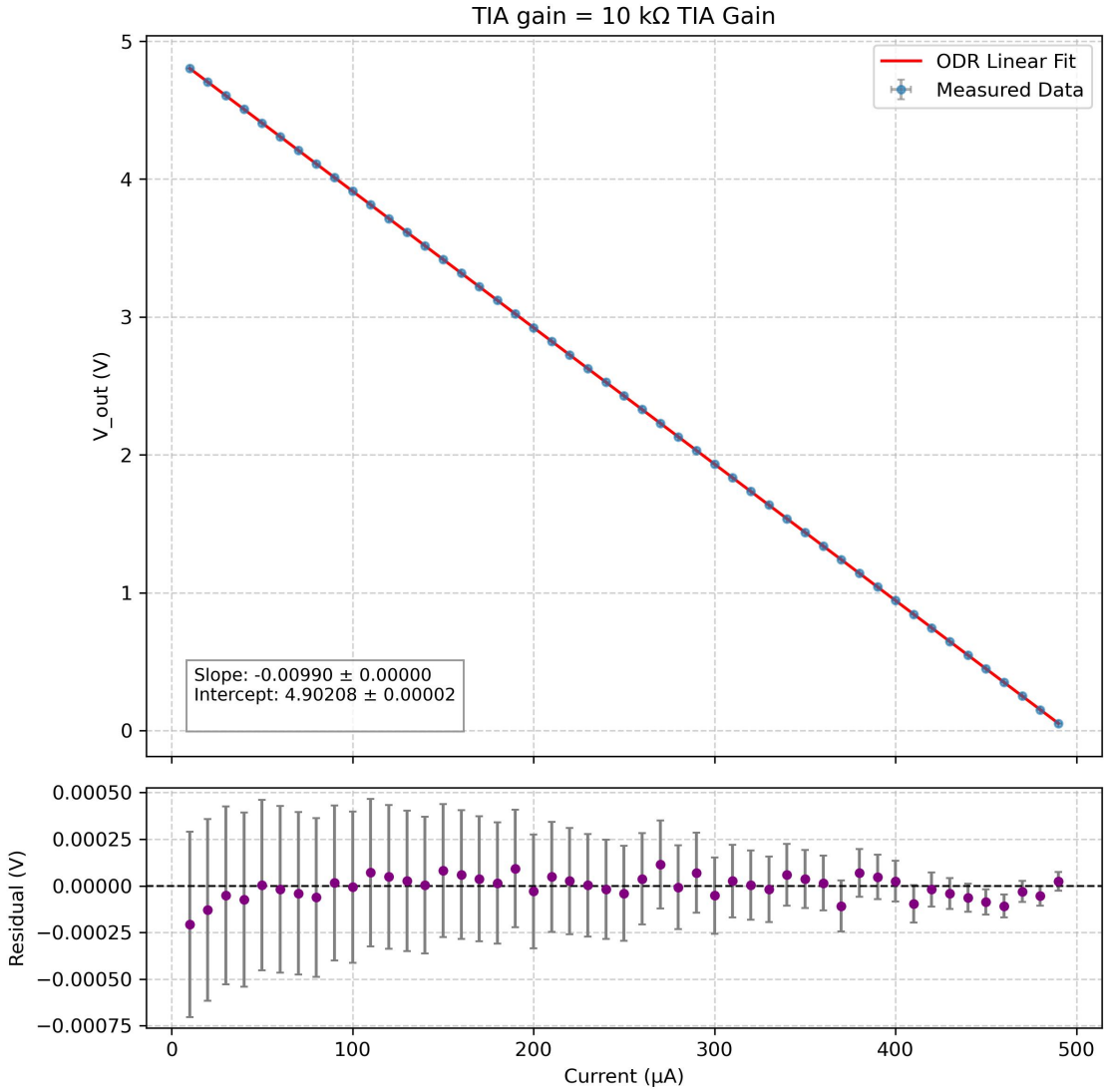

Figure 4.2: Linearity test results for the TIA circuit with a 10 kΩ gain setting. The top panel shows the measured output voltage versus input current with the ODR linear fit. The bottom panel shows the residuals.

4.2 Component Validation: PD Readout Board Integrator Linearity

While the TIA provides excellent performance for moderate photocurrents, the PD Readout board is also designed to measure extremely low light levels in the picoampere to nanoampere range. The boards utilize switched-integrator circuits that accumulate charge over a user-defined period of time, achieving a higher signal-to-noise ratio than would be possible with a TIA. This section details the experimental validation of the two integrator ICs selected for the design, the IVC102 and ACF2101, confirming their linearity and performance.

4.2.1 Experimental Methodology

The characterization of switched-integrator circuits requires a more complex methodology than for a simple TIA due to their time-dependent operation. The measurement relies on a repeating cycle of three states: resetting the integration capacitor, integrating the input current for a fixed duration, and holding the final voltage for measurement. Careful selection of the input current range and integration time is critical to ensure the integrating capacitor does not saturate and ruin the measurement.

A Teensy 4.1 microcontroller was programmed to generate the necessary digital control signals for the integrator's "RESET" and "HOLD" switches. The experimental setup utilized the dedicated test boards (Figures 3.8 and 3.9) with a Keithley 2450 Source Measurement Unit (SMU) providing a highly stable and precisely known input current. The measurement sequence executed continuously by the Teensy was as follows: first, the "RESET" switch is closed for 200μs to fully discharge the integration capacitor. Second, the "RESET" switch is opened and after a brief 10μs delay the "HOLD" switch is closed, beginning the integration period. The integrator then accumulates charge for a user defined duration. Finally, the "HOLD" switch is opened, and the integrator's output voltage is held stable. To ensure an accurate and repeatable reading, the Teensy sends a 5μs trigger pulse to the external DMM6500 precisely 5μs into this stable hold period. This hardware trigger commands the DMM to take a single, timed measurement. The output of the integrator is buffered by an LT1991 amplifier with a gain of G = -0.444 before being measured by the DMM.

Two separate tests were conducted to fully characterize the linearity: one where the input current was swept at a fixed integration time, and a second where the integration time was swept at a fixed input current.

4.2.2 Uncertainty Analysis

To accurately characterize the system, uncertainties are partitioned into "random components", which vary point-to-point and drive the observed scatter, and "correlated systematic components", which act as fixed scaling biases for a given measurement set.

Input Parameter Uncertainty

For current-sweep tests, the input uncertainty σ_I is derived from the Keithley 2450 SMU specifications (Table 4.1).

- **Random ($\sigma_{I,rand}$):** This is defined by the instrument's absolute offset floor (e.g., 100 pA on the 100 nA range). This term represents the point-to-point jitter.
- **Systematic ($\sigma_{I,sys}$):** This is the relative gain error (e.g., 0.060% on the 100 nA range). While the exact value is unknown within this tolerance, it remains fixed for all points in a sweep, creating a correlated bias rather than scatter.

Table 4.1: Keithley 2450 SMU current source accuracy specifications, as provided by the manufacturer. The total uncertainty is a combination of a relative error and an absolute floor.

Range	**Resolution**	**Accuracy: ±(% setting + amps)**
10.0000 nA	500 fA	0.100% + 100 pA
100.0000 nA	5 pA	0.060% + 150 pA
1.000000 μA	50 pA	0.025% + 400 pA

For time-sweep tests, the systematic uncertainty in integration time, $\sigma_{t,sys}$, is determined by the 30 ppm stability of the clock oscillator.

Output Voltage Uncertainty

The uncertainty in the measured output voltage, σ_V, is similarly partitioned:

- **Random ($\sigma_{V,rand}$):** Composed of the DMM6500 offset floor (50 μV) and the random thermal noise ($V_{n,rms}$) of the signal chain.
- **Systematic ($\sigma_{V,sys}$):** Includes the DMM gain accuracy (0.0025%) and the LT1991 buffer gain tolerance (0.04%).

4.2.3 Results and Evaluation

The data were analyzed using Orthogonal Distance Regression (ODR). The regression was weighted using only the "random uncertainty components" ($\sigma_{I,rand}$ and $\sigma_{V,rand}$) to ensure the fit was driven by the point-to-point noise floor. The correlated systematic errors were then propagated in quadrature with the statistical fit uncertainty for simplicity.

Linearity with Respect to Input Current

The results for the IVC102 and ACF2101 are shown in Figures 4.3 and 4.4.

The error bars reflect the total uncertainty budget (including correlated biases like buffer gain and SMU calibration), whereas the scatter is only driven by the much smaller random noise floor. The IVC102 exhibited a non-linearity of 0.0613% FSR, while the ACF2101 demonstrated 0.0436% FSR.

Linearity with Respect to Integration Time

Figures 4.5 and 4.6 show the response to integration time at a constant 100 nA. Both circuits demonstrate excellent linearity.

The IVC102 residuals (Figure 4.5) show a small deviation at short integration times < 0.5 ms, this non-linearity is likely caused by charge injection from the internal switches. However, this reduced performance at short integration scales does not affect the ALTAIR payload's operation, since the integrator channels will operate with longer integration times to accommodate Pulse Width Modulation (PWM) of the laser modules. The ACF2101 (Figure 4.6) residuals are more randomly distributed, with a non-linearity of just 0.0320% FSR. This confirms that the output of both integrator circuits scales linearly and predictably with integration time, and a slightly better performance from the ACF2101.

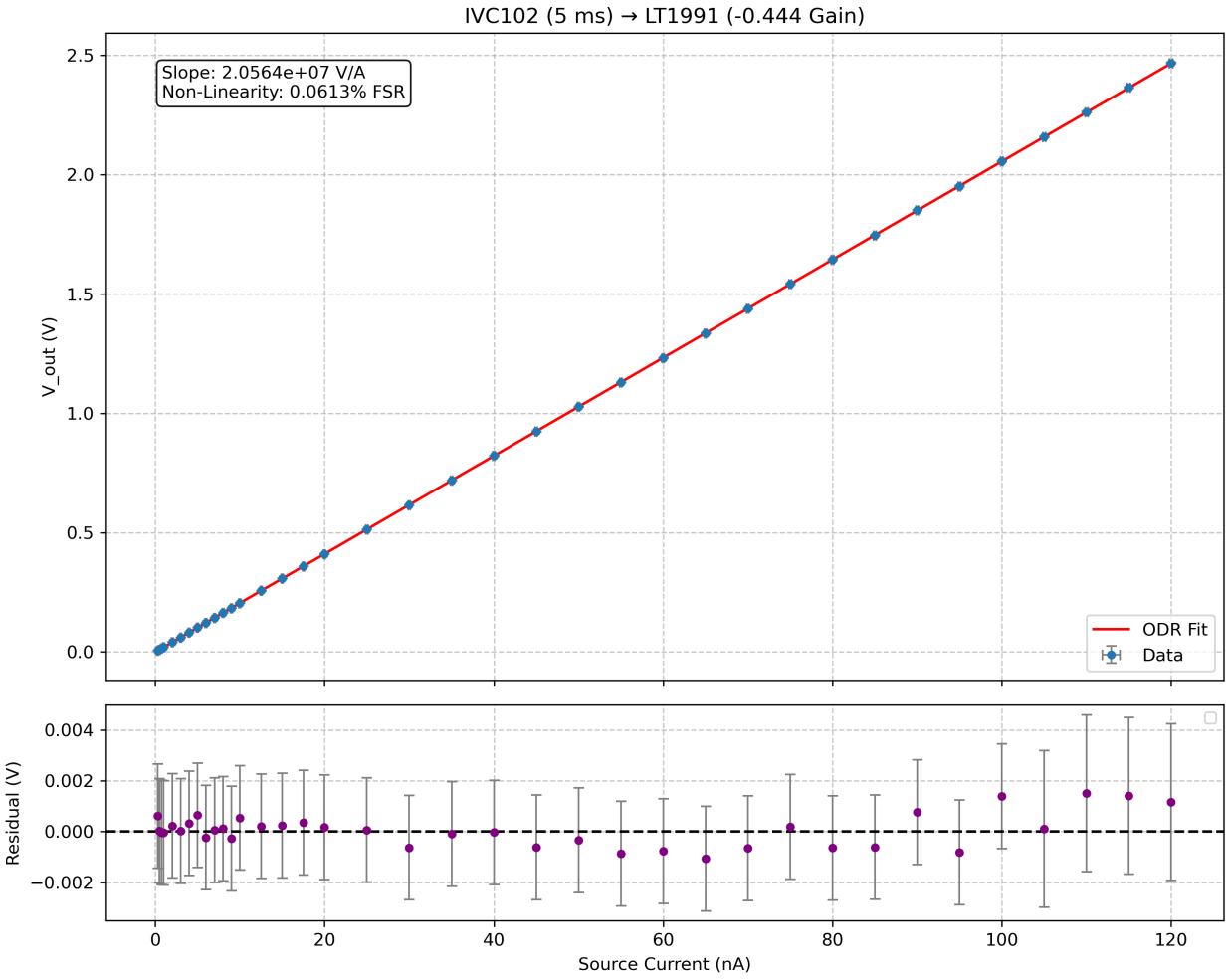

Figure 4.3: Linearity test results for the IVC102 switched integrator circuit, operated with a 5 ms integration time. The top panel shows the measured output voltage versus input source current, with the ODR fit overlaid. The bottom panel shows the residuals from the fit.

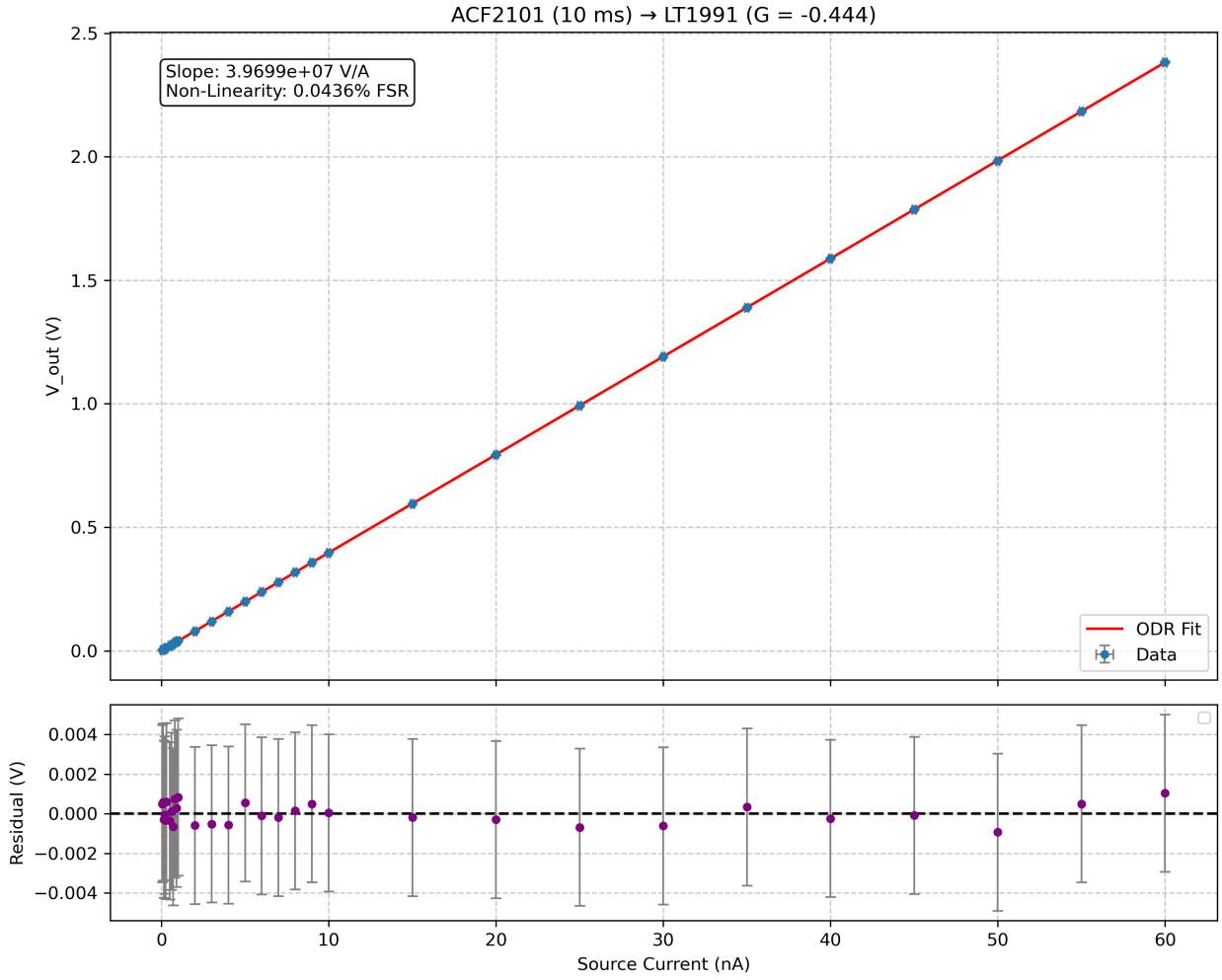

Figure 4.4: Linearity test results for the ACF2101 switched integrator circuit, operated with a 10 ms integration time. The top panel shows the measured output voltage versus input source current, with the ODR fit overlaid. The bottom panel shows the residuals from the fit.

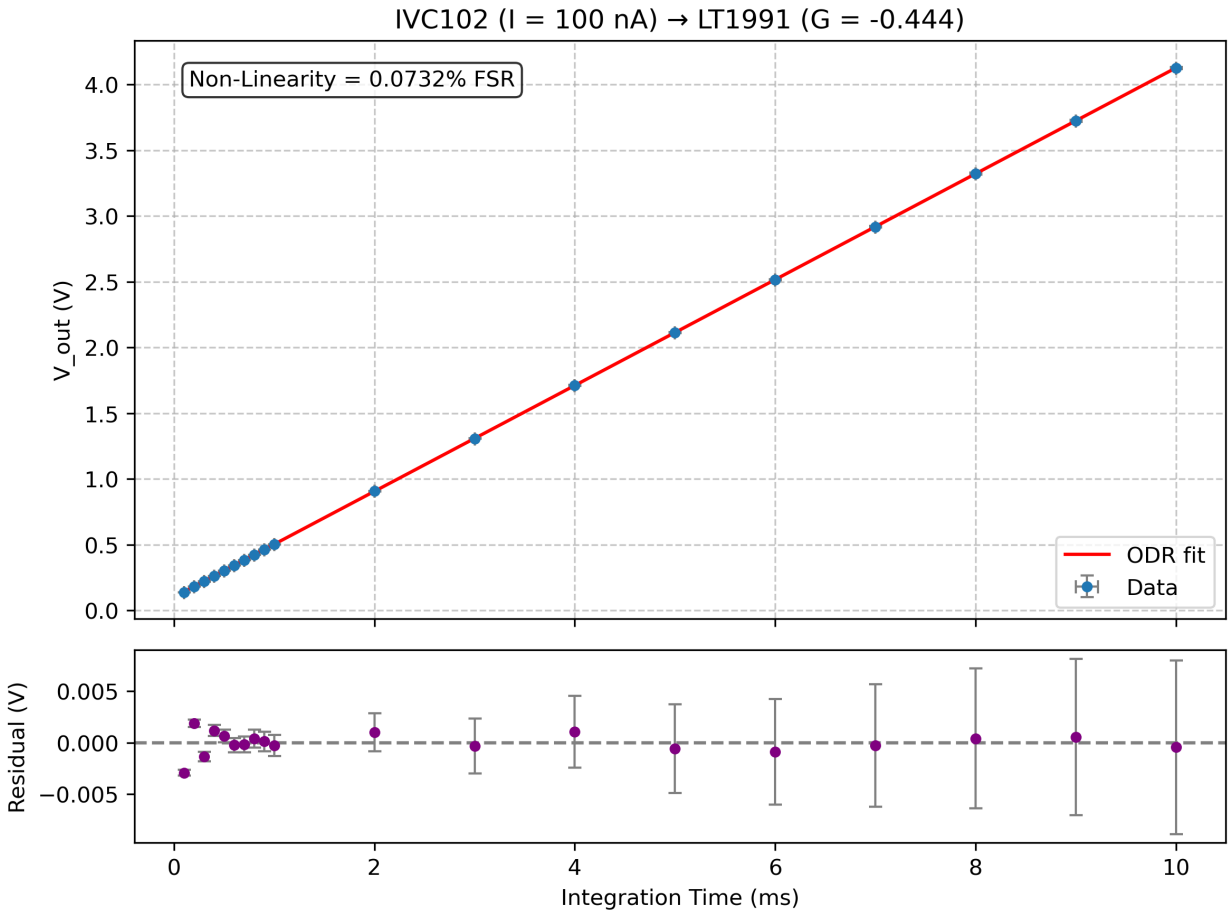

Figure 4.5: Linearity test results for the IVC102 switched integrator circuit with respect to integration time. For this test, the input current was held constant at 100 nA. The top panel shows the measured output voltage versus integration time, with the ODR fit overlaid. The bottom panel shows the residuals from the fit.

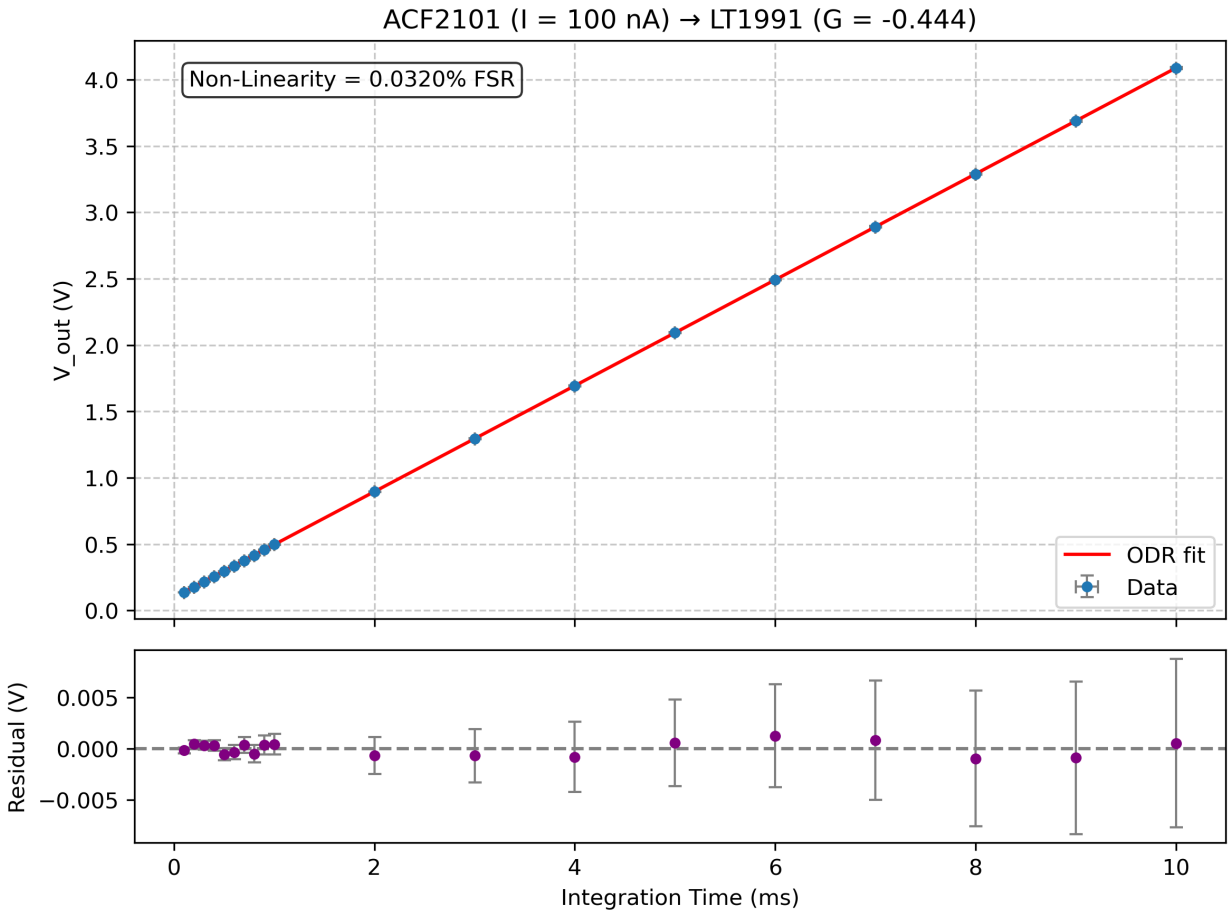

Figure 4.6: Linearity test results for the ACF2101 switched integrator circuit with respect to integration time. For this test, the input current was held constant at 100 nA. The top panel shows the measured output voltage versus integration time, with the ODR fit overlaid. The bottom panel shows the residuals from the fits.

Chapter 5

Conclusions

A high-precision photodiode readout board for the ALTAIR project was designed, produced, and tested, the design process involved a complete redesign of a prototype board to improve performance and meet space constraints of the payload. This work included the selection of critical components for low-current measurement, such as the switched-integrator integrated circuits and low thermal EMF reed relays. Dedicated test boards and experimental procedures were developed to characterize and validate these components. Low-noise PCB layout principles, such as the implementation of a guard ring for the sensitive input traces, were incorporated into the final design to mitigate sources of systematic error.

The performance of the components of the new readout board was validated through a series of laboratory tests. The transimpedance amplifier stage was demonstrated to have a deviation from linearity of less than 0.011% over its operational dynamic range. The switched-integrator circuits, critical for low-current measurements, were also characterized, exhibiting non-linearities of 0.0613% and 0.0436% of the IVC102 and ACF2101 respectively. Furthermore, thermal EMF from switching operational modes, a critical source of error in low-level DC measurements, was reduced by an order of magnitude to as low as 0.3 μV by selecting a series relay configuration based on direct experimental comparison. These results confirm that the custom electronics meet the demanding requirements for sub-percent precision photometry and validate a critical subsystem of the ALTAIR payload.

Future work should focus on the development of a comprehensive data acquisition (DAQ) software to fully automate the operation of the PD Readout board. Such software would provide an organized interface to control all aspects of the board's functionality, including the switching of input channels via the relays, generation of timing signals for the integrator reset and hold functions, the precise acquisition and logging of data from the analog-to-digital converter, and the monitoring of housekeeping data such as component and board temperatures. An automated DAQ would streamline the testing required for pre- and post-flight

validation, making an efficient characterization of the payload's performance over time and under various environmental conditions, and ensuring the long-term stability and reliability of the ALTAIR calibration.

Bibliography

[1] A. G. Riess *et al.*, "Observational Evidence from Supernovae for an Accelerating Universe and a Cosmological Constant," *The Astronomical Journal*, vol. 116, no. 3, pp. 1009–1038, 1998.

[2] S. Perlmutter *et al.*, "Measurements of Omega and Lambda from 42 High-Redshift Supernovae," *The Astrophysical Journal*, vol. 517, no. 2, pp. 565–586, 1999.

[3] The Nobel Foundation, "The nobel prize in physics 2011." https://www.nobelprize.org/prizes/physics/2011/summary/, 2011. Accessed: 2025-09-12.

[4] T. M. C. Abbott *et al.*, "First Cosmology Results using Type Ia Supernovae from the Dark Energy Survey: Constraints on the Dark Energy Equation of State," *The Astrophysical Journal Letters*, vol. 872, no. 2, p. L30, 2019.

[5] Ž. Ivezić, S. M. Kahn, J. A. Tyson, B. Abel, E. Acosta, R. Allsman, D. Alonso, Y. AlSayyad, S. F. Anderson, J. Andrew, *et al.*, "LSST: From Science Drivers to Reference Design and Anticipated Data Products," *The Astrophysical Journal*, vol. 873, no. 2, p. 44, 2019.

[6] A. Goobar and B. Leibundgut, "Supernova Cosmology: Legacy and Future," *Annual Review of Nuclear and Particle Science*, vol. 61, pp. 251–279, 2011.

[7] A. Conley, J. Guy, M. Sullivan, *et al.*, "Supernova Constraints and Systematic Uncertainties from the First Three Years of the Supernova Legacy Survey," *The Astrophysical Journal Supplement Series*, vol. 192, no. 1, p. 29, 2011.

[8] C. W. Stubbs and J. L. Tonry, "Toward 1% photometry: End-to-end calibration of astronomical telescopes and detectors," *The Astrophysical Journal*, vol. 646, no. 2, p. 1436, 2006.

Note: Although this work is foundational for modern end-to-end calibration approaches, the use of artificial reference sources predates it. Hall [39] was the first to di-

rectly calibrate stellar near-infrared measurements against a blackbody source located at the telescope. Later, tungsten ribbon-filament lamps calibrated by the National Bureau of Standards (NBS) were utilized to establish the absolute spectral energy distribution of α Lyrae [40]. There was also another significant calibration effort by D. S. Hayes [41], which established a consistent absolute flux scale for Vega by synthesizing comparisons against NBS-traceable standard lamps. In space-based efforts, the Midcourse Space Experiment (MSX) successfully used 2 cm diameter black-coated spheres ejected from the satellite as absolute infrared calibration sources [42]. While cavity blackbodies provide well-characterized radiance in the infrared, they are generally unsuitable for calibration at shorter wavelengths because the temperatures required to generate sufficient flux exceed the melting points of the cavity materials.

[9] S. Perlmutter, "Supernovae, Dark Energy, and the Accelerating Universe," *Physics Today*, vol. 56, no. 4, pp. 53–60, 2003.

[10] P. J. E. Peebles and J. T. Yu, "Primeval Adiabatic Perturbation in an Expanding Universe," *The Astrophysical Journal*, vol. 162, p. 815, dec 1970.

[11] DESI Collaboration, M. Abdul-Karim, A. G. Adame, *et al.*, "Data Release 1 of the Dark Energy Spectroscopic Instrument," *arXiv e-prints*, 2025.

[12] DESI Collaboration, J. Adame, *et al.*, "DESI 2024 VI: Cosmological Constraints from the Measurements of Baryon Acoustic Oscillations," *Journal of Cosmology and Astroparticle Physics*, 2025.

[13] G. Efstathiou, "Evolving dark energy or supernovae systematics?," *Monthly Notices of the Royal Astronomical Society*, vol. 538, no. 2, pp. 875–882, 2024.

[14] S.-F. Chen, C. Howlett, M. White, *et al.*, "Baryon acoustic oscillation theory and modelling systematics for the DESI 2024 results," *Monthly Notices of the Royal Astronomical Society*, vol. 534, no. 1, pp. 544–574, 2024.

[15] K. T. Mehta, H.-J. Seo, J. Eckel, D. J. Eisenstein, M. Metchnik, P. Pinto, and X. Xu, "Galaxy Bias and its Effects on the Baryon Acoustic Oscillations Measurements," *The Astrophysical Journal*, vol. 734, no. 2, p. 94, 2011.

[16] R. C. Bohlin, K. D. Gordon, and P.-E. Tremblay, "Techniques and Review of Absolute Flux Calibration from the Ultraviolet to the Mid-Infrared," *Publications of the Astronomical Society of the Pacific*, vol. 126, no. 942, p. 711, 2014.

[17] A. T. Young, R. M. Genet, L. J. Boyd, W. J. Borucki, G. W. Lockwood, G. W. Henry, D. S. Hall, D. P. Smith, S. L. Baliumas, R. Donahue, and D. H. Epand, "Precise Automatic Differential Stellar Photometry," *Publications of the Astronomical Society of the Pacific*, vol. 103, no. 660, p. 221, 1991.

[18] J. Albert, "Satellite-Mounted Light Sources as Photometric Calibration Standards for Ground-Based Telescopes," *The Astronomical Journal*, vol. 143, no. 1, p. 8, 2012.

[19] J. E. Albert, M. H. Fagin, Y. J. Brown, C. W. Stubbs, N. A. Kuklev, and A. J. Conley, "Precision calibration via artificial light sources above the atmophere." arxiv.org/abs/1207.1938, 2012.

[20] B. Ryden, *Introduction to Cosmology*. San Francisco, CA: Addison-Wesley, 2003.

[21] H. S. Leavitt and E. C. Pickering, "Periods of 25 Variable Stars in the Small Magellanic Cloud," *Harvard College Observatory Circular*, vol. 173, pp. 1–3, 1912.

[22] E. Hubble, "A Relation between Distance and Radial Velocity among Extra-Galactic Nebulae," *Proceedings of the National Academy of Science*, vol. 15, no. 3, pp. 168–173, 1929.

[23] G. Folatelli *et al.*, "The Carnegie Supernova Project: Analysis of the First Sample of Low-Redshift Type-Ia Supernovae," *The Astronomical Journal*, vol. 139, no. 1, p. 120, 2010.

[24] D. Scolnic *et al.*, "The Complete Light-curve Sample of Spectroscopically Confirmed SNe Ia from Pan-STARRS1 and Cosmological Constraints from the Combined Pantheon Sample," *The Astrophysical Journal*, vol. 859, no. 2, p. 101, 2018.

[25] R. Cowen, "Early observations identify star at heart of nearby supernova," *Nature*, dec 2011.

[26] M. M. Phillips, "The absolute magnitudes of Type IA supernovae," *The Astrophysical Journal*, vol. 413, pp. L105–L108, 1993.

[27] R. Tripp, "A two-parameter luminosity correction for Type IA supernovae," *Astronomy and Astrophysics*, vol. 331, pp. 815–820, 1998.

[28] J. Guy *et al.*, "SALT2: using distant Type Ia supernovae to improve the determination of the cosmological parameters," *Astronomy and Astrophysics*, vol. 466, no. 1, pp. 11–21, 2007.

[29] S. Jha, A. G. Riess, and R. P. Kirshner, "Improving the Use of Type Ia Supernovae as Cosmological Probes: The MLCS2k2 Light-Curve Fitter," *The Astrophysical Journal*, vol. 659, no. 1, p. 122, 2007.

[30] C. R. Burns *et al.*, "The Carnegie Supernova Project: Light-Curve Fitting with SNooPy," *The Astronomical Journal*, vol. 141, no. 1, p. 19, 2011.

[31] DES Collaboration, T. M. C. Abbott, *et al.*, "The dark energy survey: Cosmology results with ∼1500 new high-redshift type ia supernovae using the full 5-year dataset," *The Astrophysical Journal Letters*, vol. 973, no. 1, p. L14, 2024.

[32] D. Rubin, G. Aldering, M. Betoule, A. Fruchter, X. Huang, A. G. Kim, C. Lidman, E. Linder, S. Perlmutter, P. Ruiz-Lapuente, and N. Suzuki, "Union through unity: Cosmology with 2,000 sne using a unified bayesian framework," *The Astrophysical Journal*, 2023. arXiv:2311.12098.

[33] M. Betoule *et al.*, "Improved cosmological constraints from a joint analysis of the SDSS-II and SNLS supernova samples," *Astronomy & Astrophysics*, vol. 568, p. A22, 2014.

[34] D. Scolnic, S. Casertano, A. Riess, A. Rest, E. Schlafly, R. J. Foley, D. Finkbeiner, C. Tang, W. S. Burgett, K. C. Chambers, *et al.*, "Supercal: Cross-calibration of Multiple Photometric Systems to Improve Cosmological Measurements With Type Ia Supernovae," *The Astrophysical Journal*, vol. 815, no. 2, p. 117, 2015.

[35] Peter Plavchan, "The NASA Landolt Mission." https://youtu.be/RUEnB_jEGDI, 2023. Accessed: 2025-10-03.

[36] B. Marshall, "Guarding in multiplexer applications," Application Note SCDA042, Texas Instruments, May 2022.

[37] Pickering Electronics, "Understanding thermal emfs in reed relays." https://www.pickeringrelay.com/understanding-thermal-emfs-in-reed-relays/. Accessed: 2025-05-15.

[38] J. L. Goodeve, "Light streak photometry and streaktools," *The Astronomical Journal*, vol. 169, p. 151, feb 2025.

[39] F. F. Hall, "Measurement of stellar and planetary magnitudes in the lead sulphide region," *Infrared Information Symposium*, vol. 1, pp. 137–143, 1961.

[40] J. B. Oke and R. E. Schild, "The absolute spectral energy distribution of alpha lyrae," *The Astrophysical Journal*, vol. 161, p. 1015, 1970.

[41] D. S. Hayes, "Stellar absolute fluxes and energy distributions from 0.32 to 4.0 μm," in *Calibration of Fundamental Stellar Quantities (IAU Symposium No. 111)* (D. S. Hayes, L. E. Pasinetti, and A. G. D. Philip, eds.), (Dordrecht), pp. 225–252, Reidel, 1985.

[42] S. D. Price, C. Paxson, C. Engelke, and T. L. Murdock, "Absolute infrared calibration of standard stars by the midcourse space experiment," *The Astronomical Journal*, vol. 128, no. 2, p. 889, 2004.

Appendix A

Additional Information

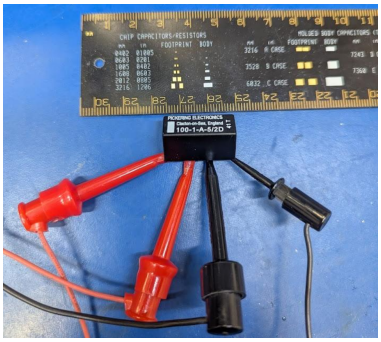

Figure A.1: The experimental setup for measuring the thermal EMF of a single Pickering 100-1-A-5/2D reed relay.

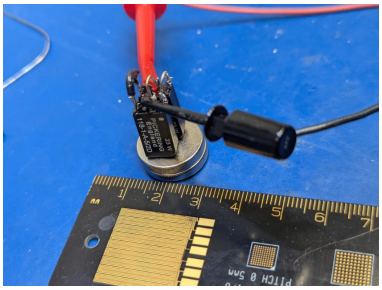

Figure A.2: The experimental setup for measuring the thermal EMF of two Pickering 118-1-A-5/2D relays, here shown in a series configuration.

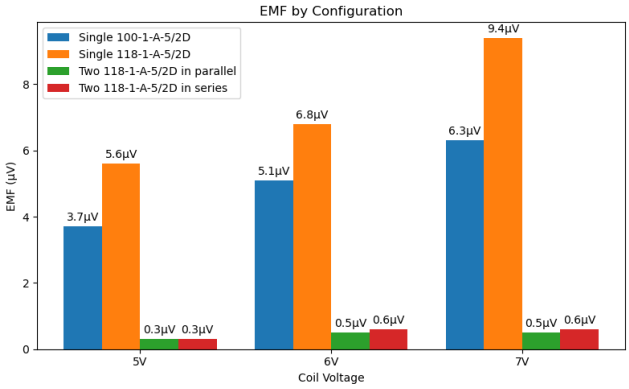

Figure A.3: Results of the thermal EMF testing for different reed relay models and configurations. The measurements, taken at various coil voltages, show that the configurations of two 118-1-A-5/2D relays consistently generates the lowest thermal EMF.